DEVELOPMENT AND VALIDATION OF A HUMAN HIP JOINT FINITE ELEMENT MODEL FOR TISSUE STRESS AND STRAIN PREDICTIONS DURING GAIT

A Thesis

presented to

the Faculty of California Polytechnic State University,

San Luis Obispo

In Partial Fulfillment

of the Requirements for the Degree

Master of Science in Mechanical Engineering

by

Jeffrey D. Pyle

December 2013

COMMITTEE MEMBERSHIP

TITLE:	Development and validation of a human hip joint finite element model for tissue stress and strain predictions during gait
AUTHOR:	Jeffrey D. Pyle
DATE SUBMITTED:	December 2013
COMMITTEE CHAIR:	Dr. Stephen Klisch, PhD Professor of Mechanical Engineering
COMMITTEE MEMBER:	Dr. Scott Hazelwood, PhD Associate Professor of Biomedical Engineering
COMMITTEE MEMBER:	Dr. Andrew Davol, PhD Professor of Mechanical Engineering

ABSTRACT

Development and validation of a human hip joint
finite element model for tissue stress
and strain predictions during gait

Jeffrey D. Pyle

Articular cartilage degeneration, called osteoarthritis, in the hip joint is a serious condition that affects millions of individuals yearly, with limited clinical solutions available to prevent or slow progression of damage. Additionally, the effects of high-risk factors (e.g. obesity, soft and hard tissue injuries, abnormal joint alignment, amputations) on the progression of osteoarthritis are not fully understood. Therefore, the objective of this thesis is to generate a finite element model for predicting osteochondral tissue stress and strain in the human hip joint during gait, with a future goal of using this model in clinically relevant studies aimed at prevention, treatment, and rehabilitation of OC injuries.

A subject specific finite element model (FEM) was developed from computerized tomography images, using rigid bones and linear elastic isotropic material properties for cartilage as a first step in model development. Peak contact pressures of 8.0 to 10.6 MPa and contact areas of 576 to 1010 mm^2 were predicted by this FEM during the stance phase of gait. This model was validated with *in vitro* measurements and found to be in good agreement with experimentally measured contact pressures, and fair agreement with measured contact areas.

Keywords: finite element, hip, articular cartilage, osteoarthritis, stance phase of gait, contact pressure, stress, strain

ACKNOWLEDGMENTS

A very special thanks to my advisors, Dr. Stephen Klisch and Dr. Scott Hazelwood, for their direction and support throughout this thesis.

Additionally, I would like to thank Dr. Andrew Anderson and Dr. Jeffrey Weiss for their help in answering questions.

I would like to thank my family and friends for their support and encouragements during graduate school.

Finally, I would especially like to thank my wife Abigail for her love and support throughout the progress of this thesis, for her help in proofreading this thesis, and her many suggestions for improvement.

This project was funded by the Extramural Funding Initiative, Cal Poly Graduate & Research Programs.

TABLE OF CONTENTS

LIST OF TABLES

LIST OF FIGURES

CHAPTER 1

Introduction

1.1 Summary

The objective of this thesis is to develop a total hip joint finite element model (FEM) for predicting cartilage and bone (i.e. osteochondral, OC) tissue stress and strain during select exercises. The long-term goal of this work is to integrate the hip joint FEM with a 3D motion analysis system and an inverse dynamic solver in order to study the effects of exercise on OC tissue stress and strain in the hip joint. Specifically, clinically relevant studies may include use of the hip joint FEM to identify and recommend exercises to prevent OC tissue damage in obese/overweight individuals, slow progression of OC tissue damage in individuals with minor asymptomatic OC defects being treated conservatively, and facilitate rehabilitation of individuals treated with surgical interventions.

A FEM of the human hip joint was developed using anatomically accurate solid models of bone and articular cartilage (hereafter referred to as cartilage). The model was developed from computed tomography (CT) data and meshed using TrueGrid (XYZ Scientific Applications, Inc., CA, USA) [1] and the Abaqus (Dassault Systemes, RI, USA) [2] pre-processor. Simulations were performed for gait and standing using joint contact loads measured *in vivo*. After model

development, model validation was performed by comparing cartilage contact pressures and areas with published data for gait loading, measured *in vitro* from subjects without defects. Contact pressures were chosen for validation due to the availability of reliable data from numerous experiments [3,4,5,6,7,8]. A future effort will apply more complex cartilage models, such as dividing cartilage into successive superficial zone, transitional zone, and deep zone layers with appropriate material properties assigned to each.

1.2 Background

1.2.1 Problem

Articular cartilage is a thin layer of connective tissue located within joints, which attaches to underlying subchondral bone via collagen fibers [9]. It functions as a low-friction, load-bearing material that facilitates normal joint motion [10,11]. Cartilage and bone degeneration leads to osteoarthritis (OA), with total direct costs of 81 billion dollars in 2003 [12]. Since overloading cartilage causes further damage [13] it is desirable to understand how certain exercises affect soft tissue stress and strain in the hip joint in order to prevent OA initiation and progression due to exercise.

In addition to focal defects or sites of degeneration serving as a high risk factor for OA, there are other risk factors that alter biomechanics and thus likely increase and/or alter cartilage loading across the joint. OA is aggravated by the increase in the number of overweight and obese individuals in the US [14,15,16]. Obesity has been shown to be a significant risk factor contributing to the

progression of OA [17,18,19,20], as an increase in weight causes changes in gait mechanics [21], and therefore may alter cartilage stress and strain, leading to initiation and progression of degeneration [22]. Therefore, it is desirable to study the effects of obesity, as well as other medical problems, on the health of cartilage in the human hip joint.

Other risks contributing to the progression of OA include minor defects in either acetabular or femoral cartilage [23,24], chondrocyte cell death [25], significant injury of the joint or nearby areas [26,20,27], or geometrical factors such as dysplasia [19,28] and femoroacetabular impingement [29], and other genetic factors [30]. In general, damage to cartilage in joints, which initiates or progresses OA, is the result of either mechanical damage, like the formation of cracks [31,32,33,34], or related to chondrocyte cell death [35,36,37] or a combination of both [38].

Various surgical techniques currently exist for treatment of OA [39]. Numerous surgical procedures attempt to repair the articular surface or restore the entire structure of cartilage [40], stimulate new growth, or graft new material in place [41]. However, many techniques are imperfect [42,39] and exercises may adversely load cartilage, damaging the recently repaired area or causing new damage in adjacent areas of cartilage due to altered and mismatched mechanical properties [43,41,44].

1.2.2 Past Work

Prior studies have used instrumented prostheses to measure *in vivo* hip joint contact loads [45,46,47,48] or cartilage contact pressures [49,47,50,51], but results were limited to gait and everyday activities, neglecting exercise important for weight loss such as bicycling, elliptical training, or running. Extensive research has gone into estimating joint contact loads through computational means for activities such as bicycling [52,53,54] and elliptical training [55,56], but to the author's knowledge, no studies have been performed to measure loads or contact pressures during these activities, either *in vitro* or *in vivo*. Additionally, since these results are general, application to the wide range of patients seen by doctors evaluating injuries is difficult, especially considering the lack of data for overweight or obese persons or other high-risk groups.

Past finite element (FE) studies have focused exclusively on gait and other everyday, non-exercise activities, using *in vivo* measured loads from a limited number of subjects [3,57,58,59,60,61], used generalized loads for parametric studies [62], or limited to individuals with very specific OC defects [63]. Additionally, many of these models made material simplifications like the use of discrete springs for cartilage representation [59,62] or constant cartilage thickness and/or spherical femoral and acetabular cartilage surfaces [59,60,61,62] that limit the models' usefulness for studying cartilage damage. A few studies have generated multiple subject-specific models, applying more accurate material models [3,57,58], but to the author's knowledge no FE studies exist which predict contact stresses or pressures for exercises important for

weight loss and conditioning/rehabilitative exercises with OA considerations. Additionally, no FE studies have been found which study the affects of obesity on joint contact. Therefore, it is necessary to develop a model with the goal of evaluating a range of cartilage stresses and strains and their distributions within the joint in order to recommend exercises to mitigate the effects of OA in high-risk groups.

1.2.3 Objective

The object of this thesis is to generate a tool for understanding and predicting OC tissue stress and strain in the human hip joint during exercise. Since *in vivo* measurements of soft tissue stresses and strains during exercise routines are often difficult to obtain, it is desirable to predict these stresses computationally in order to understand how certain movements affect soft tissue. This thesis will provide an anatomically accurate, validated FEM, which will be used in future studies with a motion analysis system and an open source musculoskeletal modeling software OpenSim (National Center for Simulation in Rehabilitation Research, Stanford University) [64] in order to produce subject-specific analysis of walking, elliptical training, and stationary bicycle training for clinically relevant studies aimed at prevention, treatment, and rehabilitation of OC injuries. Therefore, as a first step, this thesis will develop a FEM of the human hip joint to predict tissue stress and strain during the stance phase of gait.

CHAPTER 2

Methods and Materials

2.1 Subject Info

A future goal of this work is to consider effects of obesity on OC tissue stresses and strains. Therefore, data from subjects with a body mass index (BMI) corresponding to the upper end of overweight individuals were chosen (overweight = 25.0 to 29.9, obese = 30.0 and higher). A subject's BMI can be calculated as follows [65]:

$$BMI = \frac{weight\ (kg)}{[height\ (m)]^2}$$

Since *in vivo* joint contact force data were measured using an instrumented hip prosthesis, it was necessary to obtain joint contact forces and natural hip joint geometry from separate subjects. Research has shown that obese persons alter their gait patterns in order to reduce loads on the knee joints [66,67,7], so subjects were chosen which have a similar BMI for good agreement between hip kinematic and kinetic data and hip geometry. Basic information for these subjects can be seen in Table **1**.

Table 1. Information from subjects used in this thesis. Both subjects fall within the "overweight" range of BMI (BMI = weight(kg)/[height(m)]^2).

Subject	Data	Sex	Age (y)	Height (cm)	Weight (kg)	BMI
JOR10 [68]	CT Images	F	21	165	80	29.4
HSR [45]	Angles/Loads	M	55	174	87.67	29.0

2.2 Structures Included

The bones included in the model are the femur and the acetabulum (the cup-shaped region of the pelvis surrounding the femoral head). Only the proximal femur is modeled, with the appropriate joint reaction forces applied at the joint center. Since bone is roughly 1000 times stiffer than cartilage, bones were modeled as rigid bodies, greatly reducing computational time. Since bones were modeled as rigid, only the outer surface of the bone was processed, since the outer surface is sufficient for a rigid body definition in Abaqus. Additionally, only the acetabulum was included since the additional geometry of the ilium and ischium does not contribute to the accuracy of the solution. The cartilage tissues included are the acetabular and femoral articular cartilage. Cartilage material properties are described in more detail below. Justifications for omitted soft tissues are also presented.

2.3 Cartilage Material Properties

Extensive research has resulted in the development of accurate material models for cartilage. Researchers suggest everything from simple linear elastic isotropic properties [69] to incompressible, neo-Hookean hyperelastic models [3]. In most cases, cartilage was modeled as incompressible, or nearly

incompressible [3,57,70,59,71]. Although cartilage is more accurately described as an anisotropic, nonlinear biphasic poroelastic material, research indicates that for short loading times such as occurs during most daily activities including gait (< 0.5 s), cartilage can be described by its instantaneous elastic modulus [72,32,73,74]. Additionally, homogenous isotropic properties greatly reduce simulation times while still having been found to produce results comparable to measured *in vitro* pressures. Therefore, linear elastic isotropic properties are applied.

Since gait and exercises exhibit short joint loading times, elastic properties that correspond to instantaneous cartilage properties were used, as opposed to equilibrium values, measured experimentally during very short loading times. Cartilage was specified as a homogeneous isotropic solid, with the elastic modulus of the acetabular cartilage set to 19.3 MPa and the elastic modulus of the femoral cartilage at 14.6 MPa, which are consistent with values measured experimentally in research [58], other FE modeling efforts [3,71], and suggested in literature [75]. Values found in other FE studies and past experiments for Poisson's ratio generally varied from around 0.45 to 0.5 [70,76,71,57]. Therefore, a nearly incompressible Poisson's ratio of 0.495 was chosen for reasonable consistency with other models.

2.4 Ligaments and Other Soft Tissues

Ligaments provide stabilization to joints and restrict movement to prevent injury and damage from over-extension, and extensive research has measured

the contribution of each ligament to the range of motion in the hip [77]. The hip joint is a ball-and-socket joint and relatively more stable than other joints. Numerous ligaments surrounding the hip joint provide additional stabilization, limiting range-of-motion and preventing dislocations. While this concept is fairly well understood, there is significant disagreement as to how these ligaments contribute individually to the stabilization, as well as how to distinguish and identify them from one another [78]. However, since this model aims to predict cartilage stresses during activities within the normal range of motion, ligaments were not included. Furthermore, since this model uses loads measured *in vivo*, any contribution ligaments have in developing contact loads are inherently included in the experimental data. Additionally, muscles were not modeled, since load data used also included their contribution.

In consideration of the extent of the acetabular cartilage boundary, the labrum is generally recognized as functioning to maintain hydrostatic fluid pressurization during loading [79], in order to maintain lower friction between cartilage surfaces [80,81], and support higher loads without damage [82]. Although past research shows a greater role of the labrum in supporting contact loads [83], more recent studies suggest the labrum does not contribute significantly to the contact pressures and areas under normal loading in normal human hips [84,85]. Additionally, any loads imposed by the labrum on the joint contact force are inherently included in the load data. Therefore the labrum was not included in the model for simplicity at this phase of model.

2.5 Solid Geometry Development

Although a publicly available FEM of the hip joint has not been found, publicly available CT scans were located (discussed below), which provide a good starting point for model development. A careful process of geometry development, mesh generation, and model validation was implemented in order to develop an anatomically accurate, validated FEM. These modeling parameters and processes are examined further in the following subsections.

2.5.1 Computerized Tomography Image Processing

The computerized tomography (CT) images made available by the Musculoskeletal Research Laboratories at the University of Utah [68] were used to develop the solid models and FE meshes for this thesis. CT data were available for 10 subjects, so a subject which matches the BMI of a subject for which instrumented hip joint contact forces is available was chosen. CT images were obtained using the following methods [51]. First, traction was applied to one of the subject's hip joints and then a contrast agent was injected into the joint in order to provide a contrasted separation of the cartilage surfaces. Next, the hip region was scanned with a multi-detector CT scanner. In total, 3,795 images were acquired for the subject chosen, with 723 in the axial plane and 1,536 each in the sagittal and coronal planes. For reference, for a subject standing in a neutral position, the axial plane is parallel to the ground, the sagittal plane divides the subject left and right, and the coronal plane divides the subject in posterior and anterior. An example image from the CT data from which bone and cartilage geometry were obtained is shown in Figure **1**.

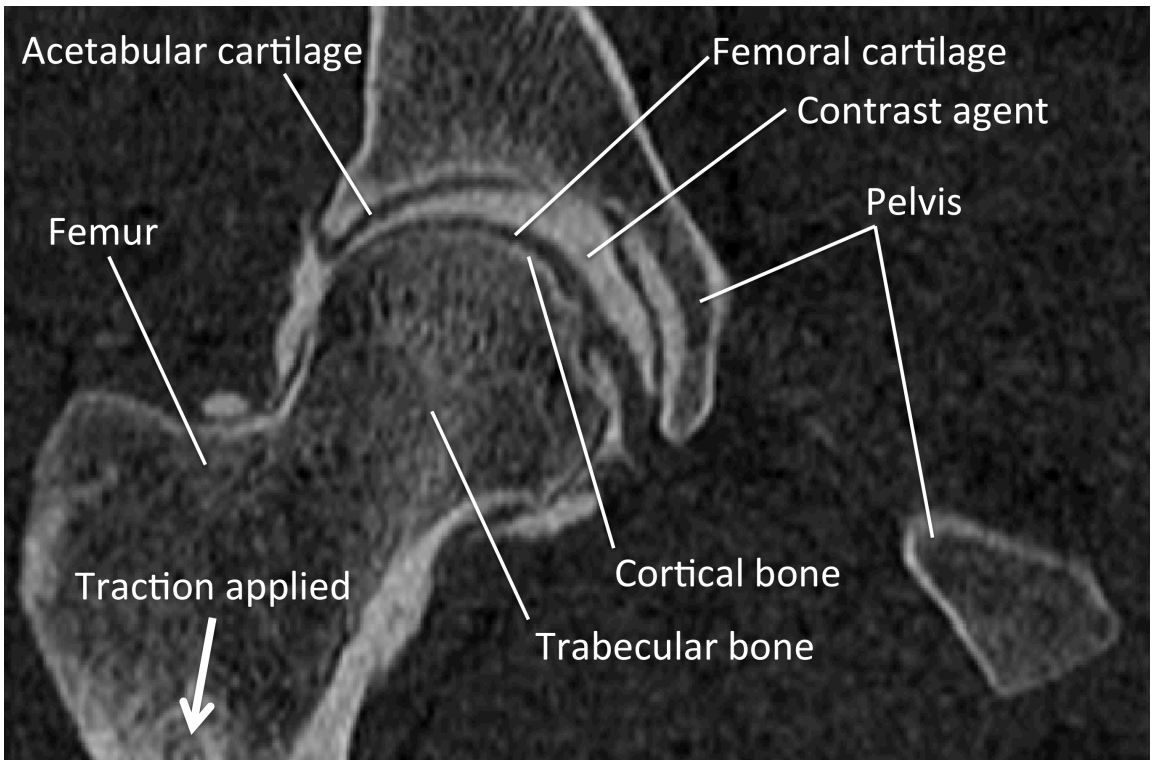

Figure 1. CT image used for bone and cartilage geometry definition, showing traction with contrast agent injected for cartilage surface distinction. Sagittal scan from CT scans available from University of Utah Musculoskeletal Research Laboratories [68].

The CT images used for the development of this model were imported into Mimics (Materialise, Leuven, Belgium) [86] image processing software for development of a solid model. Since CT images use a grayscale pixel range, lower density tissues such as cartilage appear on the black end of the scale and higher density tissues such as cortical bone appear on the white end of the scale. A threshold profile was developed in order to minimize the manual masking required to separate trabecular bone, cortical bone, cartilage, and contrast agent into different regions. This threshold profile was created by selecting an upper

and lower grayscale value bounding a range of values that most accurately describe dense tissues (e.g. cortical bone). A “mask” was then created using the threshold profile, which is the process of coloring regions in which the grayscale values fall within the range of the threshold values. Trial and error was used in attempt to create a mask that requires minimal manual coloring of areas that fall outside the range of values, but should still be included. Since the contrast agent and cortical bone have very similar grayscale values, in areas in which the contrast agent comes into contact with cortical bones, the boundary was estimated and masks manually separated by erasing a narrow portion of the contrast agent mask, leaving a distinct cortical bone boundary.

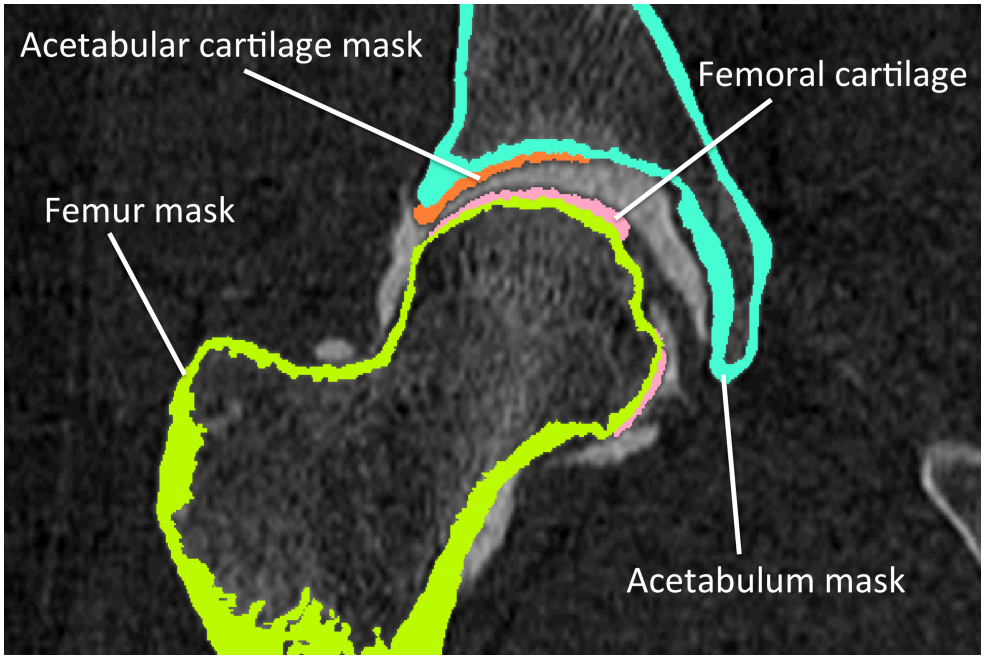

Figure 2. Anatomical masks were specified to represent each tissue. STL files were generated from each individual mask and exported for further processing.

Next, a solid, 3-dimensional part was generated for each mask, and a process called “smoothing” was applied in order to smooth the surfaces and eliminate imperfections due to difficulties in masking lower contrast CT scans. This process attempts to smooth both high and low spots in geometry in order to remove artifacts created by the masking process. After sufficient smoothing, the geometry was examined in order to locate high or low spots that were too large to be properly smoothed. The mask was then edited manually in these areas in order to remove these artifacts. Smoothing parameters are found in Table **2**.

Table 2. MIMICS smoothing parameters used for the smoothing operation performed on each biological tissue. Default parameters were used when not listed below.

	# Iterations	Factor
Femur, Outer Surface	60	0.800
Femur, Inner Surface	100	0.800
Cartilage, Femoral	50	0.800
Pelvis	500	0.800
Cartilage, Acetabular	200	0.800

In addition to smoothing, a process called “Triangle reduction” was used in order to reduce the number of elements representing the outer surface. This process reduces the number of triangular surface elements used to describe the acetabulum geometry in order to preserve memory and improve graphics performance. The acetabulum was reduced using an edge reduction mode with a tolerance of 0.4 mm, an edge angle of 15°, and the number of iterations set to 100. Smoothed solid bodies were exported as stereo lithography (STL) files for conversion to surfaces in the computer aided design (CAD) software SolidWorks

(Dassault Systemes, CA, USA) [87] or in the case of the pelvis, directly as a surface mesh into Abaqus.

2.5.2 Solid Model Surface Processing

The STL files were imported into SolidWorks for surface processing. STL files define only the surface of 3-dimensional geometry using connected triangles, also called a surface mesh. SolidWorks contains tools for using these surface meshes to generate SolidWorks surfaces, which it defines using mathematical equations. The STL parts were each converted to surfaces by allowing the automatic surface generation tool to attempt to create surfaces matching the mesh geometry. However, since bone and cartilage surfaces are generally complex shapes, manual sectioning of the mesh with surface boundary lines on the surface mesh was often necessary in order to force the tool to find a better solution when some sections failed to generate surfaces or created surfaces with obvious errors. This process was then iterated until geometry was produced that, upon close inspection, contained no missing surfaces or tangential mismatches between adjacent surfaces, where two surfaces have different slopes where they connect.

Next, the outer edges of the surfaces were visually trimmed with the “surface cut” tool since surface approximations often deviated significantly from the imported STL part, causing wavy or curled edges that are not representative of actual joint geometry (see Figure **3**).

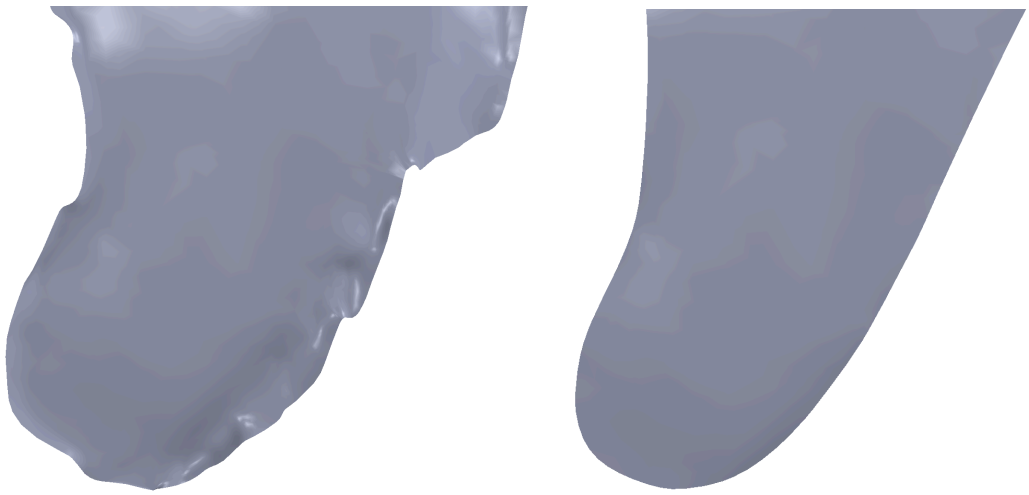

Figure 3. SolidWorks model of the articulating surface of the anterior region of acetabular cartilage showing rough edges from the imported STL file before trimming (left) and after trimming (right).

The surfaces were then aligned with a local coordinate system so that the femur can be oriented and loads applied properly. Both the femoral and pelvic coordinate systems are adaptations of the ones used in the OrthoLoad database [45], from which loads used in this thesis were obtained. The femur was aligned such that the X-axis is parallel to the ground and positive towards the medial direction, the Y-axis extends toward the posterior, and the Z-axis extends cranially. The pelvis was aligned similarly, with the center of each acetabulum socket along the X-axis and the center of the L5-S1 vertebrae joint aligned in the X-Z plane. A graphical representation of this coordinate system can be seen in Figure **4**.

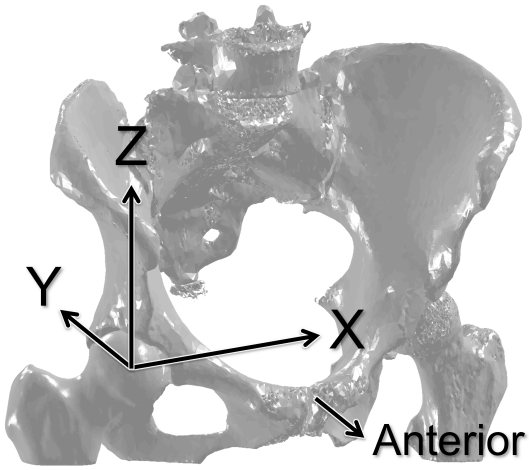

Figure 4. Coordinate system used in model, with origin at the center of the right femoral head, with X parallel to the ground and positive in medial direction, Y extending toward the posterior, and Z extends cranially.

Next, each surface model was manually sectioned into four-sided patches and edge curves were created in order to make meshing easier and more accurate. This provides edges to which computation mesh element edges can be assigned, as well as a surface to which a face of a computational mesh element can be assigned. A picture of the sectioned femur can be seen in Figure **5**.

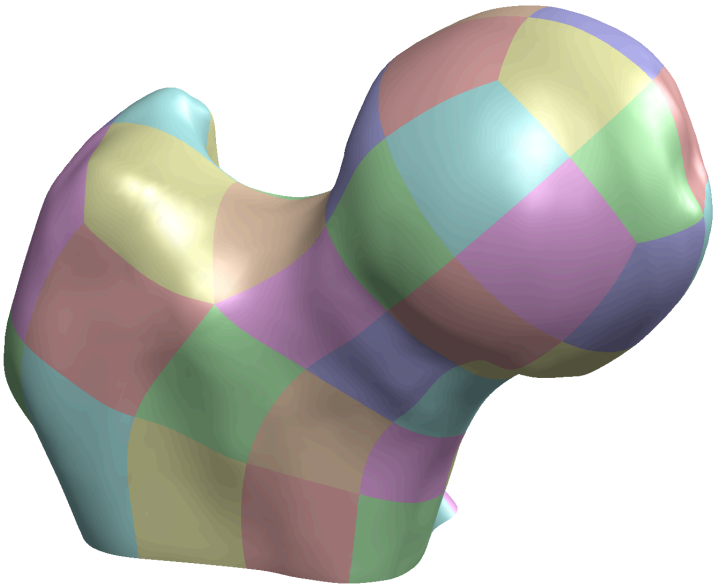

Figure 5. SolidWorks model of proximal femur showing the manual sectioning of the surface into 4-sided patches to aid mesh development (colored for distinction).

2.6 Mesh Development

TrueGrid was used for meshing of both femoral and acetabular cartilage as well as the femur bone surface. A computational mesh (a simple mesh which can be manipulated to conform to geometry and refined to produce the final mesh, see Figure **6**) was generated, and its edges were attached to the appropriate edges of each of the surface patches defined in SolidWorks.

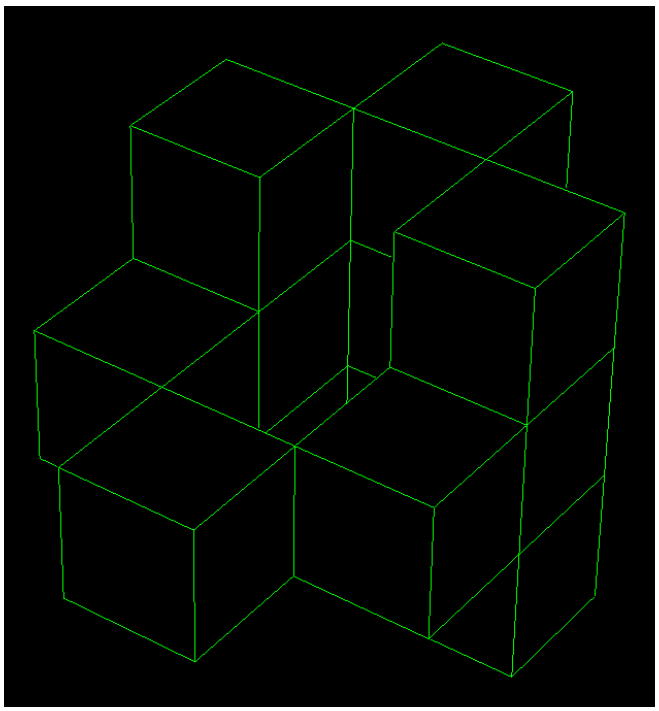

Figure 6. A computational mesh defined in TrueGrid for meshing the femoral cartilage. Edges and faces of this computational mesh were projected to curves and surfaces defined in SolidWorks.

The faces of the computational mesh were projected to the corresponding surface patches and the mesh was appropriately refined. An image of a partially projected mesh can be seen in Figure **7**. Surface and node sets for contact and tie constraints were then defined before generation of the input file for importing the mesh into Abaqus.

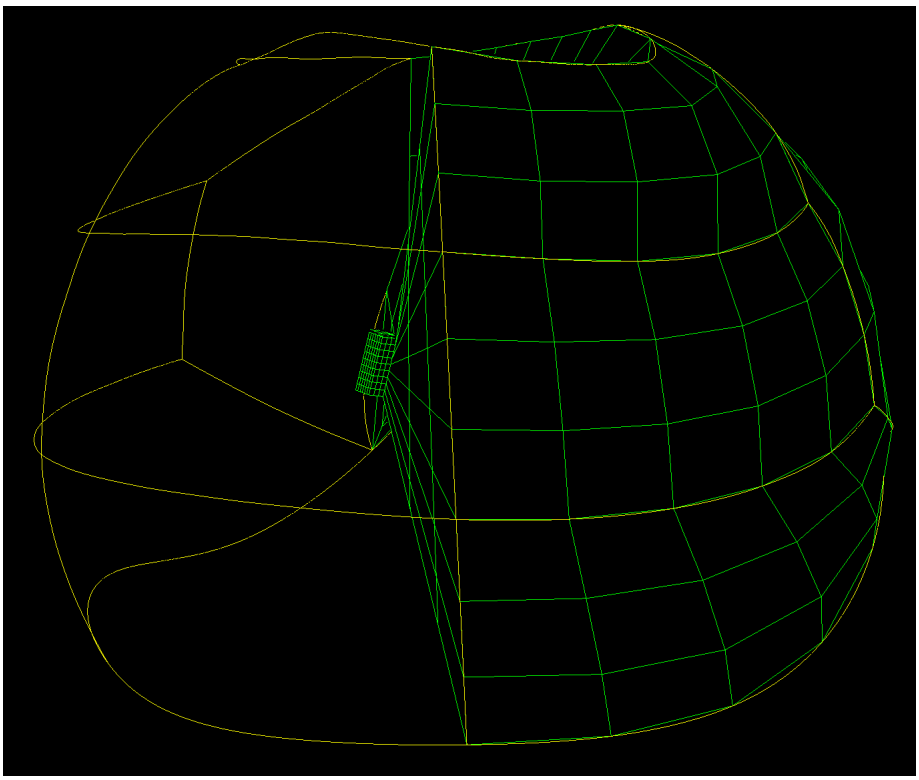

Figure 7. Partially projected mesh defined in TrueGrid. Yellow lines represent curves defined in SolidWorks, and green lines represent the mesh, with minor refinement added.

Some iteration of the surface patch definition in SolidWorks and mesh generation in TrueGrid was necessary in order to improve areas where high curvature caused difficulties in producing a sufficiently high quality mesh. Ideally, surface patches will be equilateral and edges orthogonal to one another, yielding a high quality mesh having good element edge aspect ratios and edges that are close to orthogonal to one another. However, complex surface shapes require some deviation from this, and a convergence study helps ensure accurate results.

Because of the very complex shape of the acetabulum, it was imported directly into Abaqus as an STL surface mesh with only minimal mesh editing required within the Abaqus pre-processor. Areas of the mesh that were pinched or bridged were manually corrected by deleting elements, then creating new elements in order to smooth the area. Sequential rotations of 6.33 degrees about the X-axis, 6.26 degrees about the Y-axis, and -6.74 degrees about the Z-axis were applied in order to align the pelvis with the coordinate system described in the OrthoLoad database [45]. A surface element set was manually defined with elements where the acetabular cartilage attaches to subchondral bone to define the acetabular cartilage tie constraint, detailed in a following section.

Both cartilage sections are modeled with linear hexahedral elements. The femur was modeled with rigid quadrilateral surface elements, and the acetabulum was modeled with rigid triangular surface elements. Meshes of the femur and acetabulum separately can be seen in Figure **8**, and the full hip joint can be seen in Figure **9**. Some element information for each mesh can be seen in Table **3**.

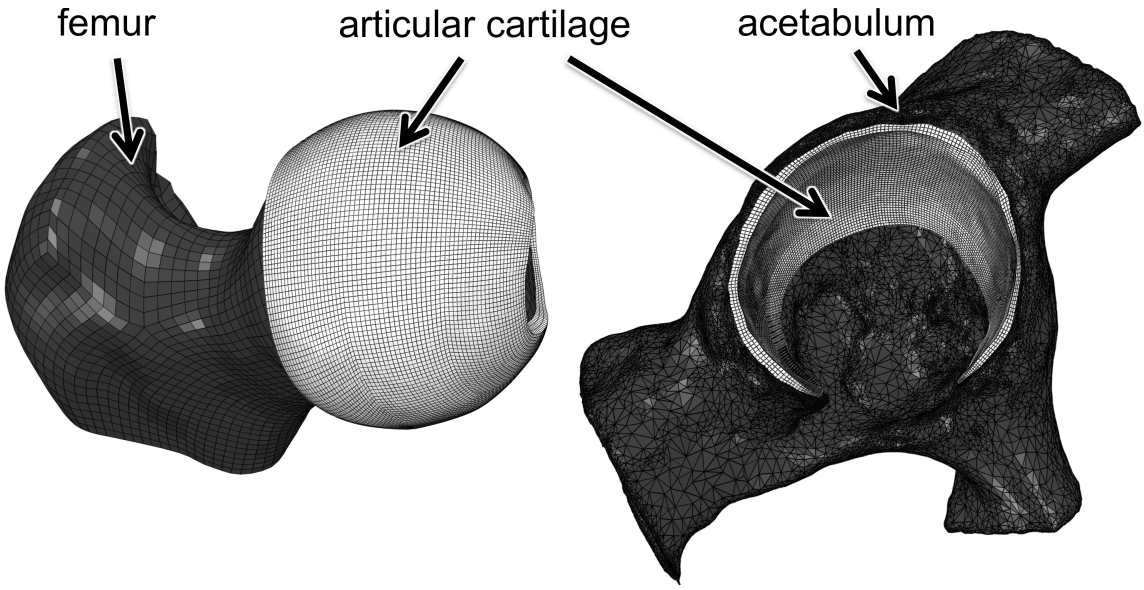

Figure 8. Converged mesh of femur and femoral cartilage (left) and acetabulum and acetabular cartilage (right). Bones are shown in dark gray, and articular cartilage is shown in light gray.

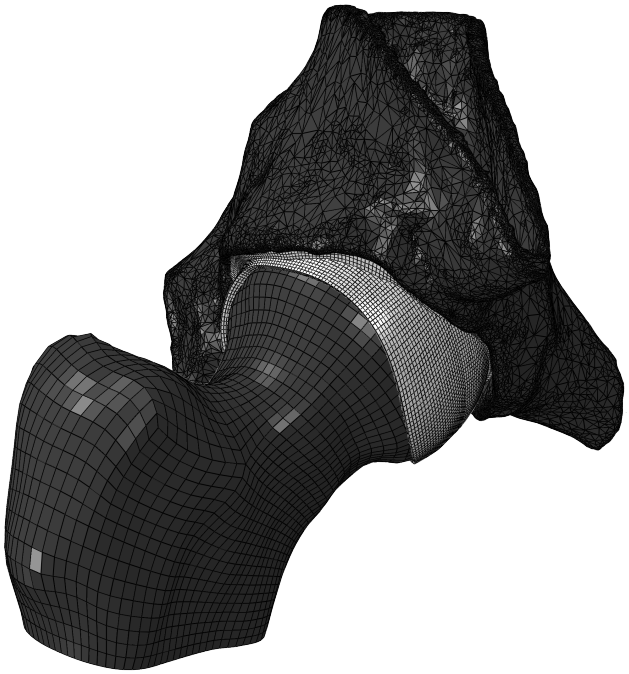

Figure 9. Full hip joint converged mesh showing bone in dark gray and articular cartilage in light gray.

Table 3. Element information for each section.

	# of Elements	Element Type	Designation
Cartilage, Acetabular	26,484	Hexahedral, linear	C3D8
Cartilage, Femoral	29,940	Hexahedral, linear	C3D8
Femur	3,200	Quadrilateral, rigid	R3D4
Pelvis	101,169	Triangular, rigid	R3D3

2.7 Finite Element Modeling

Abaqus FE software is a powerful, commercially available FE solver with both a pre- and post-processor that can be used to generate FEMs and analyze a variety of complex geometries. In addition, it provides tools for generating meshes, as well as versatile customizable user subroutines for defining custom materials. These subroutines will be utilized in future studies to add more complex material models to the FEM. Abaqus is used as the FEM solver and post-processor to view and analyze the results of these simulations.

Upon generating a mesh, a set of quasi-static equilibrium analyses were performed to begin the model validation process. For this thesis, a quasi-static equilibrium analysis takes the dynamic hip joint contact load measured *in vivo* at a single point in time and treats it as static, developing reaction forces and moments on the fixed boundary conditions. Since these loads already include the inertial forces for each of the bodies, which are necessary to bring a dynamic model into quasi-static equilibrium, they can be applied as if the model is static at a specific point in time. This assumption allows the use of instrumented hip implant loads to develop a series of static FEM simulations as opposed to performing a true dynamic FE simulation. Additionally, the quasi-static

assumption is a well-established method, used in numerous FEMs of the hip and knee joints [59,70].

2.7.1 Computer Specifications

All simulations run in this thesis were performed on two custom-built workstations with an Intel core i7-950 3.06 GHz quad-core processor computer running the Linux Fedora version 10 operating system with an ASUS P6X58D premium motherboard and 12 GB RAM. Run times ranged from 40.7 to 54.1 minutes wall clock time (4.3 to 5.8 hours CPU time) for all simulations performed in this thesis.

2.7.2 Boundary Conditions and Loads

The pelvis was specified as a discrete rigid body, with a reference point created near the center of the acetabulum. The pelvis was fixed in all six degrees of freedom (DOF) at the rigid body reference point as required by Abaqus. The femur was also set as a discrete rigid body, with translation DOF's free and a rotational DOF's fixed to the relative angles of the femur with respect to the pelvis, as seen in Table **4**. Angles for each of the eight load cases examined were determined from the file "HSRWN0" from the OrthoLoad database [45].

Although Abaqus warns against using displacement boundary conditions and recommends applying angular velocities for a one second period of time to specify large, multi-axis rotations for multi-step, 3-dimensional models, it was determined that applying fixed angular displacements resulted in no orientation

difference than applying angular velocities. Therefore, fixed angular displacements were used for model simplicity.

Table 4. Relative angles between the femur and pelvis at select instances during the stance phase of gait and standing. These angles are from file “HSRWN0” from the OrthoLoad database [45].

Position	Flexion (deg)	Abduction (deg)	Internal Rotation (deg)
Gait, 0% Stance	-29.7	4.31	-1.02
Gait, 5% Stance	-27.8	2.16	-0.27
Gait, 13.5% Stance (Peak load)	-21.4	-2.58	3.48
Gait, 25% Stance	-10.5	-6.79	8.08
Gait, 50% Stance	8.65	-3.33	16.8
Gait, 75% Stance	-15.9	9.17	12.8
Gait, 100% Stance	-28.4	4.11	1.81
Standing	4.32	6.62	6.95

Loads were defined as a concentrated force described relative to the femoral reference frame used to describe the load [46] and applied at a reference point located in the center of the femoral head, which correlates to the theoretical joint center. This point is consistent with the description of the experimentally measured joint contact loads in the OrthoLoad database [45]. Since the hip is a ball-and-socket joint, negligible moments are transmitted between cartilage surfaces and were ignored for this analysis. The loads used for each time point of the stance can be seen in Table **5**.

Table 5. Joint contact loads at select time points during the stance phase of gait, relative to the femoral coordinate system. These loads are from file “HSRWN0” from the OrthoLoad database [45], with the exception of the resultant, which was calculated from the X, Y, and Z components of the load.

Position	Fx (N)	Fy (N)	Fz (N)	Resultant (N)
Gait, 0% Stance	302	5.18	938	986
Gait, 5% Stance	383	-69.2	1440	1490
Gait, 13.5% Stance (Peak load)	403	-247	2070	2130
Gait, 25% Stance	366	-164	1560	1610
Gait, 50% Stance	218	13.4	1570	1580
Gait, 75% Stance	193	85.3	375	431
Gait, 100% Stance	309	19.1	940	989
Standing	226	74.2	662	703

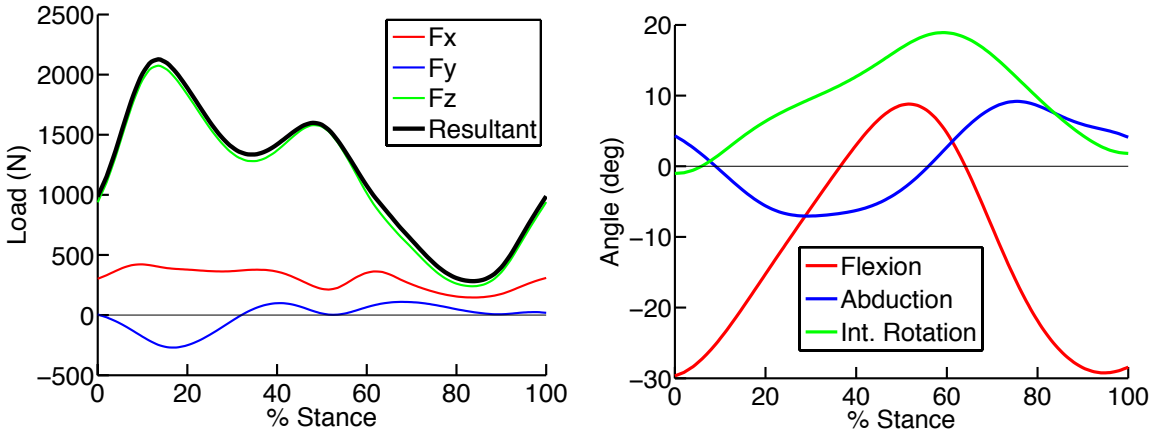

Figure 10. Plots of load (left) and relative position of femur with respect to pelvis (right) during stance phase of gait.

2.7.3 Cartilage Attachment Constraints

A node-to-surface tie constraint was specified between both the cartilage meshes and their respective cortical bone surfaces. This type of constraint is appropriate since collagen fibers anchor cartilage securely to subchondral bone [9]. For the tie constraint definition, the bone surface was defined as the master

surface and cartilage surface nodes as the slave nodes. Since hexahedral elements do not have rotational DOF's, they were not tied between the meshes. The slave nodes were not adjusted, since moving their position to lie directly on the surface would result in greatly skewed elements in some cases. However, the position tolerance was increased to 2.1 mm for both femoral and acetabular tie constraints so that all nodes of the slave surface would be tied to their respective surfaces on bone.

2.7.4 Contact Interaction Definition

Contact between cartilage surfaces was defined using a surface-to-surface contact interaction. Surface-to-surface contact minimizes master surface penetration into the slave surface while also avoiding uneven stress distribution at slave nodes. Finite sliding was specified since it allows non-linear contact with greater sliding. No slave adjustment, surface smoothing, or contact stabilization was used. Since much of the load is supported by fluid pressure during short load times [82] resulting in very low friction [88], the contact was defined as frictionless. This is appropriate since the very low coefficient of kinetic friction—on the order of 0.003-0.01—would not develop significant tangential loading on the cartilage.

2.7.5 Analysis Steps

A total of five steps were used to simulate loading the joint. All steps were static, general steps with non-linear geometry turned on. For non-load steps, no automatic stabilization was used. For loaded steps, a non-adaptive damping

factor of 0.001 was specified to enable convergence. The steps were specified as seen in Table **6**.

Table 6. Analysis step descriptions.

	Analysis Step				
Boundary Condition/Load	1: Initial	2: Set_Femur_Angle	3: Dislocate	4: Setting_Load	5: Apply_Load
BC: Fix all pelvis DOF's	Created	Propogated	Propogated	Propogated	Propogated
BC: Set Femur Rotational DOF's		Created	Propogated	Propogated	Propogated
BC: Fix Femur in Translation		Created	Inactive	Inactive	Inactive
BC: Apply small translation to Femur			Created	Inactive	Inactive
Load: Apply small load to Femur				Created	Inactive
Load: Apply full static load to Femur					Created

The *Initial* step only specifies pelvis boundary conditions. The *Set_Femur_Angle* step specifies the prescribed rotations on the femur, holding them constant for the rest of the simulation. In addition, the translation DOF's are set as zero while rotations are applied for this step only. The *Dislocate* step applies a small translation in the form of translational velocities for a time period of one second. This step has the effect of withdrawing the femoral head from the acetabulum in order to ensure the contact surfaces do not begin the step penetrating one another. The *Setting_Load* step initiates the contact interaction, applying a small load to the femur in order to force the femoral head into the acetabulum, positioning it in very light contact in preparation for the final, full load step. This small load is only applied at this step. The final *Apply_Load* step is

used for the application of the full quasi-static load. The femur is free to translate at this step, and is only constrained in the rotational DOF's as applied in the *Set_Femur_Angle* step. Results are reported for output variables at the final increment of the *Apply_Load* step.

2.7.6 Output Variables

The following standard output variables were selected for output at the last increment of the final step: contact pressure (CPRESS), contact area (CNAREA), and logarithmic strain (LE). In addition to these variables, it is desirable to compare Green-Lagrange maximum principal and maximum shear strains with published data regarding cartilage damage [89,31]. However, since Abaqus only outputs logarithmic strain for geometrically non-linear problems, a UVARM subroutine was utilized in order to convert maximum and minimum principal and maximum shear logarithmic strains to the equivalent Green-Lagrange strain. F is defined as the deformation gradient tensor.

The left Cauchy-Green deformation tensor, B, and the right Cauchy-Green deformation tensor, C, are defined as:

$$B = F \cdot F^T$$

$$C = F^T \cdot F$$

and are both symmetric positive-definite tensors. The polar decomposition theorem yields:

$$F = RU = VR$$

where R is a proper orthogonal rotation tensor and U and V are symmetric positive-definite right and left stretch tensors, respectively. Using the polar decomposition of F, tensors B and C can be expressed as

$$B = V^2$$

$$C = U^2$$

Logarithmic strain, ε_L, and Green-Lagrange strain, ε_G, are defined as:

$$\varepsilon_L = ln\, V$$

$$\varepsilon_G = \frac{1}{2}(C - I)$$

Using the spectral decomposition theorem for symmetric positive-definite tensors, B and C can be defined in their eigenbases as:

$$B = \sum_{i=1}^{3} {\lambda_i}^2 n_i \otimes n_i$$

$$C = \sum_{i=1}^{3} {\lambda_i}^2 N_i \otimes N_i$$

where the principal stretches λ_i are the same for both B and C, N_i represent eigenvectors in the reference configuration, and n_i represent eigenvectors in the current configuration. Substituting, V is represented as:

$$V = \sum_{i=1}^{3} \lambda_i n_i \otimes n_i$$

Therefore, both ε_L and ε_G can be defined in terms of principal stretches:

$$\varepsilon_{Li} = \ln \lambda_i$$

$$\varepsilon_{Gi} = \frac{1}{2}\left({\lambda_i}^2 - 1\right)$$

and principal values of logarithmic strain can then be used to calculate principal values of Green-Lagrange strain:

$$\varepsilon_{Gi} = \frac{1}{2}((e^{\varepsilon_{L}\,i})^2 - 1)$$

Maximum shear Green-Lagrange strains were calculated using:

$$\gamma_G = \frac{\varepsilon_{G,max} - \varepsilon_{G,min}}{2}$$

where $\varepsilon_{G,max}$ is the maximum principal Green-Lagrange strain and $\varepsilon_{G,min}$ is the minimum principal Green-Lagrange strain. A UVARM custom variable subroutine was created using these equations and used to output Green-Lagrange strain for cartilage. The subroutine can be found in

APPENDICES

Appendix A: User subroutine to define principal Green-Lagrange strains.

2.8 Mesh Convergence

2.8.1 Articular Cartilage Meshes

In order to verify that a properly refined mesh was used, producing accurate results while minimizing simulation times, a mesh convergence study was performed on both cartilage meshes. A series of meshes were generated with increasing density for the study. Nodes to query for the mesh convergence were defined at corners of the computational mesh, locations where the coordinates of the node remain constant during mesh refinements. A total of six nodes were defined for the acetabular cartilage, and eight for the femoral cartilage. Each cartilage convergence study was performed separately; one cartilage mesh was progressively refined, and a series of simulations were performed while the other cartilage mesh was held constant at a medium-density mesh. The highest hip joint resultant load and its associated femur flexion, abduction, and inward rotation angles were used for the mesh convergence study. These loads and angles can be seen in Table **7**.

Table 7. Peak gait loads and femur position angles used for mesh convergence study, from file “HSRWN0” from the OrthoLoad database [45]. 13.5% stance was chosen because the resultant force was greatest at this point of the gait cycle.

	13.5 % stance (Peak load)
Fx (N)	403
Fy (N)	-247
Fz (N)	2070
Flexion (deg)	-21.4
Abduction (deg)	-2.58
Rotation (deg)	-3.48

After the finest mesh simulation was run, each of the convergence nodes were queried, and the three highest contact pressures from both femoral and acetabular cartilage were noted and then used to judge convergence. The plots of these six nodes can be seen below, with the results of sufficiently refined mesh plotted to demonstrate mesh convergence.

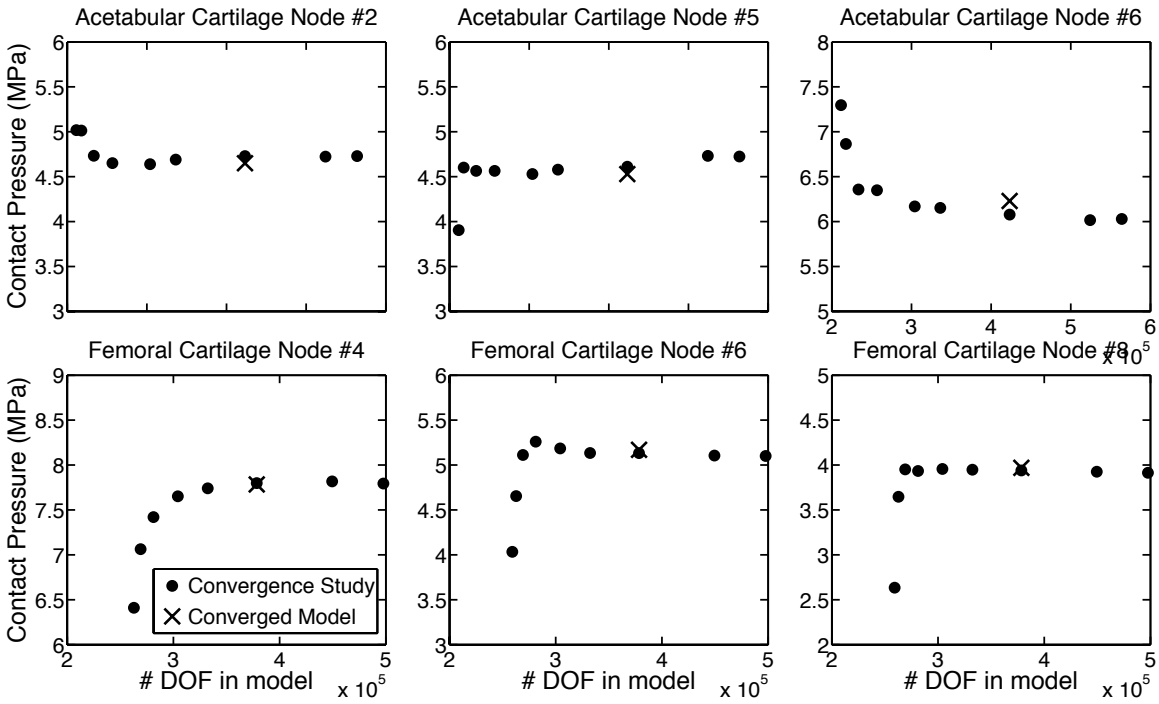

Figure 11. Mesh convergence study shows convergence for peak hip loading during normal gait for acetabular cartilage (top) and femoral cartilage (bottom). The individual meshes selected for the convergence study are plotted with dots, and the final model containing the converged meshes are plotted with X's.

Although the femoral cartilage converges more quickly than the acetabular cartilage, a slightly higher quality mesh was chosen in order to more closely match the quality of acetabular cartilage necessary for accurate results. A picture of the mesh for both femoral and acetabular cartilage can be seen in Figure **9**.

Both femoral and acetabular cartilage show good convergence with the mesh quality chosen. Contact pressures from the converged model show good agreement with the converged values reported by the finest mesh quality model, with less than 2.5% difference. A possible explanation for this small discrepancy is that the acetabular mesh used for the convergence studies was slightly too

coarse to develop consistent results in the femoral cartilage. However, this is not a concern since the difference is small.

The converged acetabular cartilage contains 26,484 elements and the femoral cartilage contains 29,940 elements for a total of 56,424 deformable elements. Both the femoral cartilage and acetabular cartilage contain three elements through the thickness. A total of 497,544 variables were generated in the model for simulation, which includes all free DOFs, as well as additional variables required for contact.

2.8.2 Femur and Pelvis Meshes

For the scope of this thesis, bone was represented as rigid surfaces. The pelvis was trimmed in order to simplify mesh development. At least 25 millimeters of the pelvis was retained around the acetabulum for the FEM, measured from the edge of acetabular cartilage. The mesh density was reduced, as described in the Mesh Development section.

The femur was meshed such that sufficient surface detail was retained for an accurate tie constraint definition. Since a surface mesh is adequate to define rigid bodies in Abaqus, only the external surface of the femur was meshed.

2.9 Damping Factor Convergence

Problems involving surface-to-surface contact often pose solution convergence difficulties and require stabilization in order to find an accurate solution. The solver incrementally applies the load while predicting the displacements corresponding to the current increment. It then iterates, attempting

to refine its prediction until it's close enough to proceed to the next load increment. For unstable problems like this model, the displacement predictions can depart quickly from actual displacements and the solver will be unable to converge. In order to slow down the progression of these displacement predictions, stabilization applies viscous forces to unstable nodes so the solver can converge on a solution. Stabilization can be applied to any unstable analysis steps by specifying a damping factor that controls the amount of stabilization Abaqus applies.

Since stabilization affects the ability of the solver to find a solution, the time required to arrive at a solution, and the accuracy of that solution, an optimum damping factor is desired. This ensures that an accurate solution can be achieved while still minimizing computation time. Automatic stabilization with a constant damping factor was used since other automatic stabilization techniques were not effective likely due to the relatively large deformations during application of displacement boundary conditions and cartilage deformation during contact that the FEM undergoes.

In order to ensure the model is not over-damped, thus generating an inaccurate solution, the Abaqus analysis manual recommends comparing nodal viscous forces to total forces. A study was run in which contact pressure at each of the nodes used in the mesh convergence study was measured. The following plot shows the convergence of each selected node with a dashed line representing a value that is 1% of the converged value.

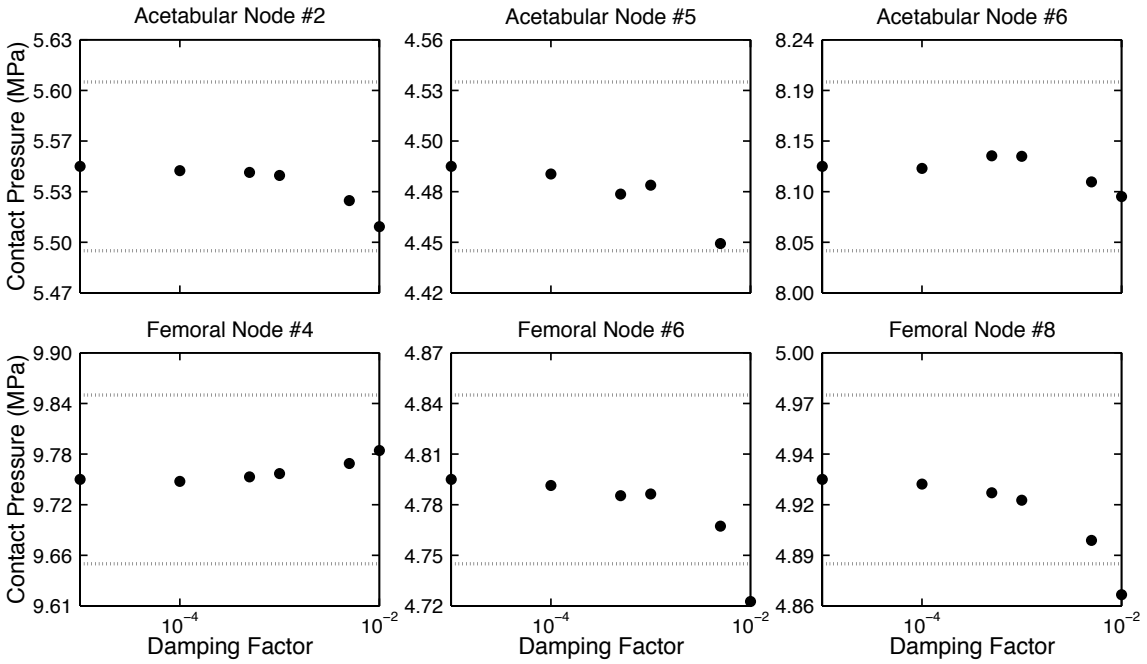

Figure 12. Damping factor convergence study showing converged results with decreasing damping factor specified. The dashed line represents a contact pressure value that is 1% of the final converged value. Results for simulations with damping factors above 10^{-2} omitted since contact pressures were zero for most nodes.

In addition to plotting the pressures at various nodes, a comparison was made to verify the range of the percentage of viscous forces of total forces and their corresponding damping factors in order to determine a good starting point for the damping factor for each model. It can be seen in Figure **13** that the solution quickly diverges near a damping factor of 0.1.

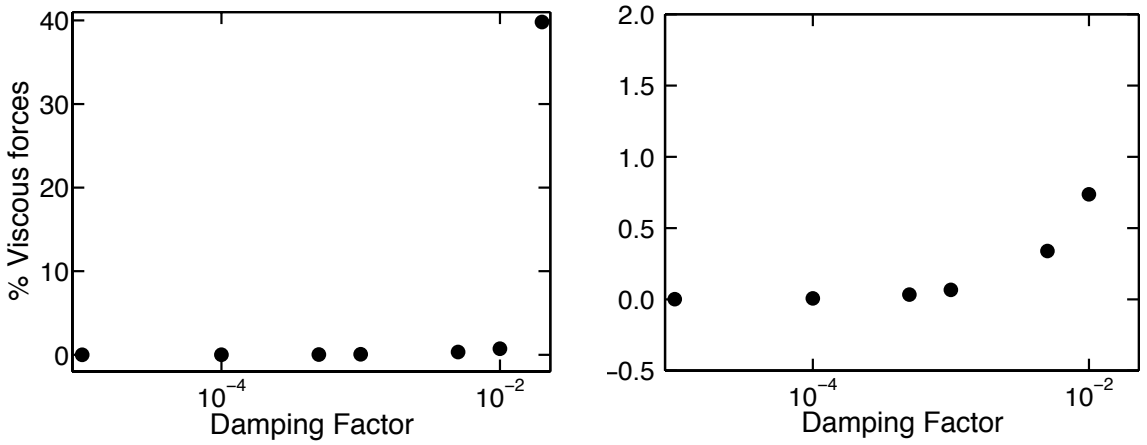

Figure 13. Percentage of viscous forces to total forces and their corresponding damping factors. A dramatic change occurs in this model and the solution diverges quickly near 10^{-2} (left). All damping factors used in this model fall within the range of factors producing a percentage viscous forces of total forces near 1% (right).

This damping factor correlates well with the damping factor at which contact pressures diverge quickly. Therefore, a factor of 0.01 was chosen as a starting point for each model. After running the final simulations, the percentage of viscous forces was calculated for each simulation in order to verify that viscous forces are small relative to the total forces in the model. All viscous forces were found to be close to 1% of the total forces, verifying that each simulation is not over-damped.

Table 8. List of viscous forces, total forces, and damping factors used for each simulation.

Forces (N)	Stance Phase of Gait							
	0%	5%	13.5% (Peak load)	25%	50%	75%	100%	Standing
Total Forces	986	1490	2130	1610	1580	431	990	703
Viscous Forces	11.4	14.8	14.8	12.0	17.1	4.81	11.6	5.48
% of Total	1.2	1.0	0.7	0.7	1.1	1.1	1.2	0.8
Damping Factor Used	0.008	0.01	0.01	0.008	0.007	0.003	0.008	0.005

CHAPTER 3

Results

In general, results depend on % stance phase of gait cycle, with higher values for contact pressure and Green-Lagrange strains correlating to higher loads. Contour plots for contact pressure, maximum principal strains, and maximum shear strains can be seen at the end of this section.

Peak contact pressures ranging from 8.0 MPa to 10.6 MPa were observed for the 75% stance (the lowest load) and 13.5% stance (peak load) cases respectively. Contact area for these cases were 576 mm^2 and 1010 mm^2. At some time points, peak contact pressures occurred on the femoral cartilage at the edge of the acetabular cartilage. However, this is most likely an artifact and is discussed further in the Discussion section. A table of results with peak contact pressures and contact areas for each time point in stance, as well as standing, can be seen in Table **9**, with contour plots shown in Figure **14**.

Table 9. Peak contact pressures and contact areas recorded for each time point (% stance phase of gait cycle), as well as for standing.

	Stance Phase of Gait							
	0%	5%	13.5% (Peak load)	25%	50%	75%	100%	Standing
Resultant Load (N)	986	1490	2130	1610	1580	431	990	703
Contact Pressure (MPa)	9.0	9.9	10.6	9.7	10.0	8.0	9.5	8.5
Contact Area (mm^2)	840	958	1010	930	842	576	835	777

Maximum principal strains were generally found to be below 10%. Peak strains in the acetabular cartilage exceeded 147% in the anterior region for 100% stance, with peak strains of 39% in the femoral cartilage. However, these peak strains are likely the result of an underrepresentation of cartilage thickness (see Discussion), and more realistic peak predictions of 19% and 26% were observed in acetabular and femoral cartilage respectively. A table of results with peak maximum principal Green-Lagrange strains for each time point in stance, as well as standing, can be seen in Table **10**, with contour plots shown in Figure **15**.

Table 10. Peak maximum principal Green-Lagrange strains recorded for each time point (% stance phase of gait cycle), as well as for standing.

	Stance Phase of Gait							
	0%	5%	13.5% (Peak load)	25%	50%	75%	100%	Standing
Acetabular Cartilage (max reported)	1.241	1.320	1.109	0.853	1.432	1.046	1.256	1.477
Acetabular Cartilage (true max)	0.117	0.149	0.192	0.142	0.196	0.115	0.132	0.090
Femoral Cartilage (max reported)	0.391	0.327	0.298	0.287	0.279	0.226	0.299	0.247
Femoral Cartilage (true max)	0.154	0.235	0.264	0.244	0.256	0.157	0.162	0.156

Maximum shear strains were also generally found to be below 10% for the highest load cases. The peak strain recorded in the acetabular cartilage was 100% for standing, with the peak strain in the femoral cartilage recorded as 34%. These peak strains are also likely the result of inaccurate cartilage geometry (discussed further in Discussion). More realistic predictions of peak strains were 17% in the acetabular cartilage and 22% in the femoral cartilage. A table of results with peak maximum shear Green-Lagrange strains for each time point in stance, as well as standing, can be seen in Table **11**, with contour plots shown in Figure **16**.

Table 11. Peak maximum shear Green-Lagrange strains recorded for each time point (% stance phase of gait cycle), as well as for standing.

	Stance Phase of Gait							
	0%	5%	13.5% (Peak load)	25%	50%	75%	100%	Standing
Acetabular Cartilage (max reported)	0.871	0.916	0.804	0.651	0.978	0.769	0.880	1.005
Acetabular Cartilage (true max)	0.107	0.134	0.167	0.130	0.171	0.105	0.119	0.084
Femoral Cartilage (max reported)	0.335	0.265	0.244	0.237	0.233	0.194	0.247	0.210
Femoral Cartilage (true max)	0.137	0.201	0.222	0.208	0.215	0.140	0.144	0.139

A table of results for minimum principal Green-Lagrange strain can be found in Appendix B: Table of minimum principal Green-Lagrange strain. Simulation times for these results ranged from 40.7 to 54.1 minutes wall clock time. CPU times for these simulations ranged from 4.3 hours to 5.8 hours.

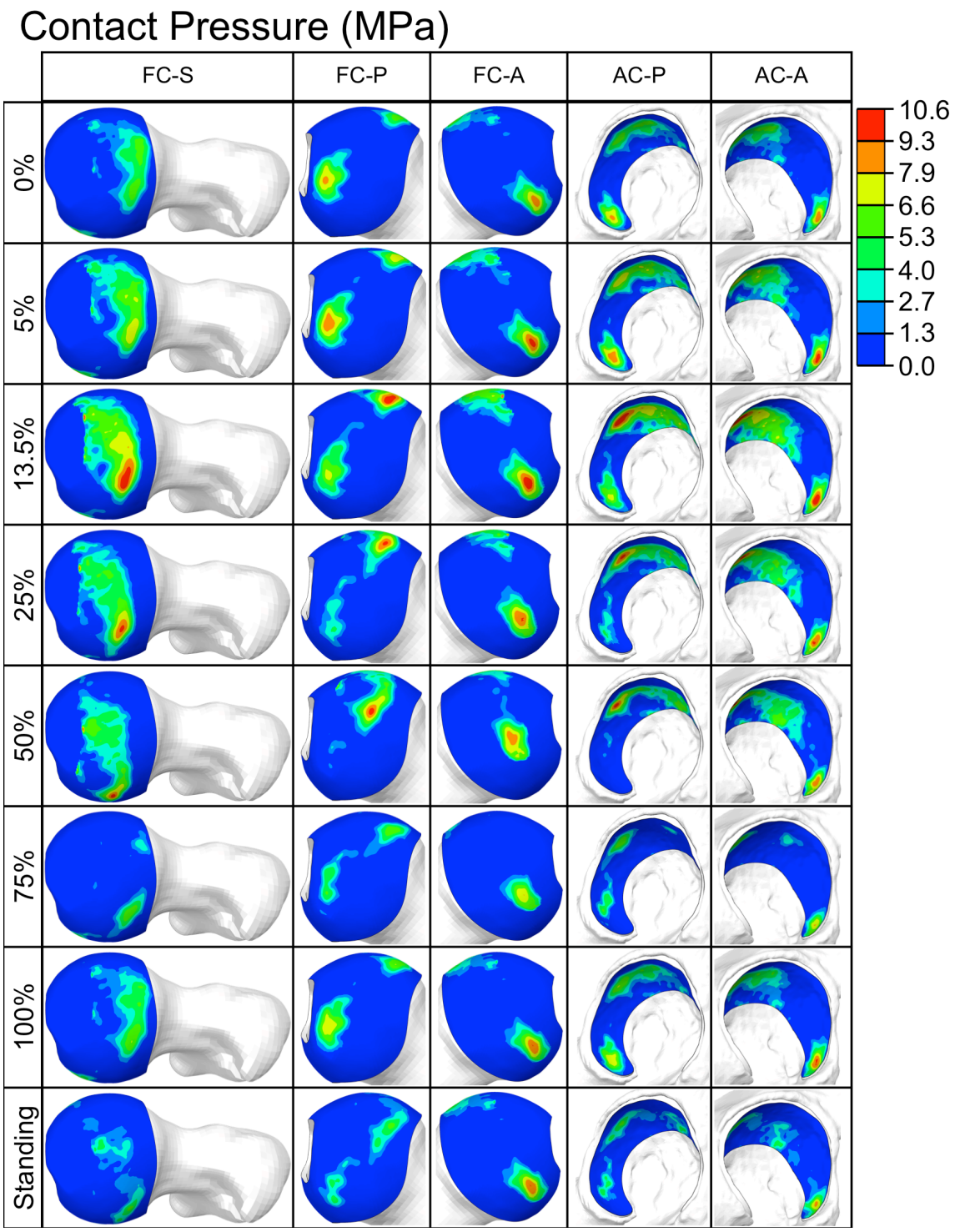

Figure 14. Contour plots of contact pressure at seven time points (% stance phase of gait cycle) and one for standing. Femoral cartilage is shown in superior (FC-S), posterior (FC-P), and anterior (FC-A) views and acetabular cartilage is shown in posterior (AC-P) and anterior (AC-A) views demonstrating a change in contact depending on % gait and standing.

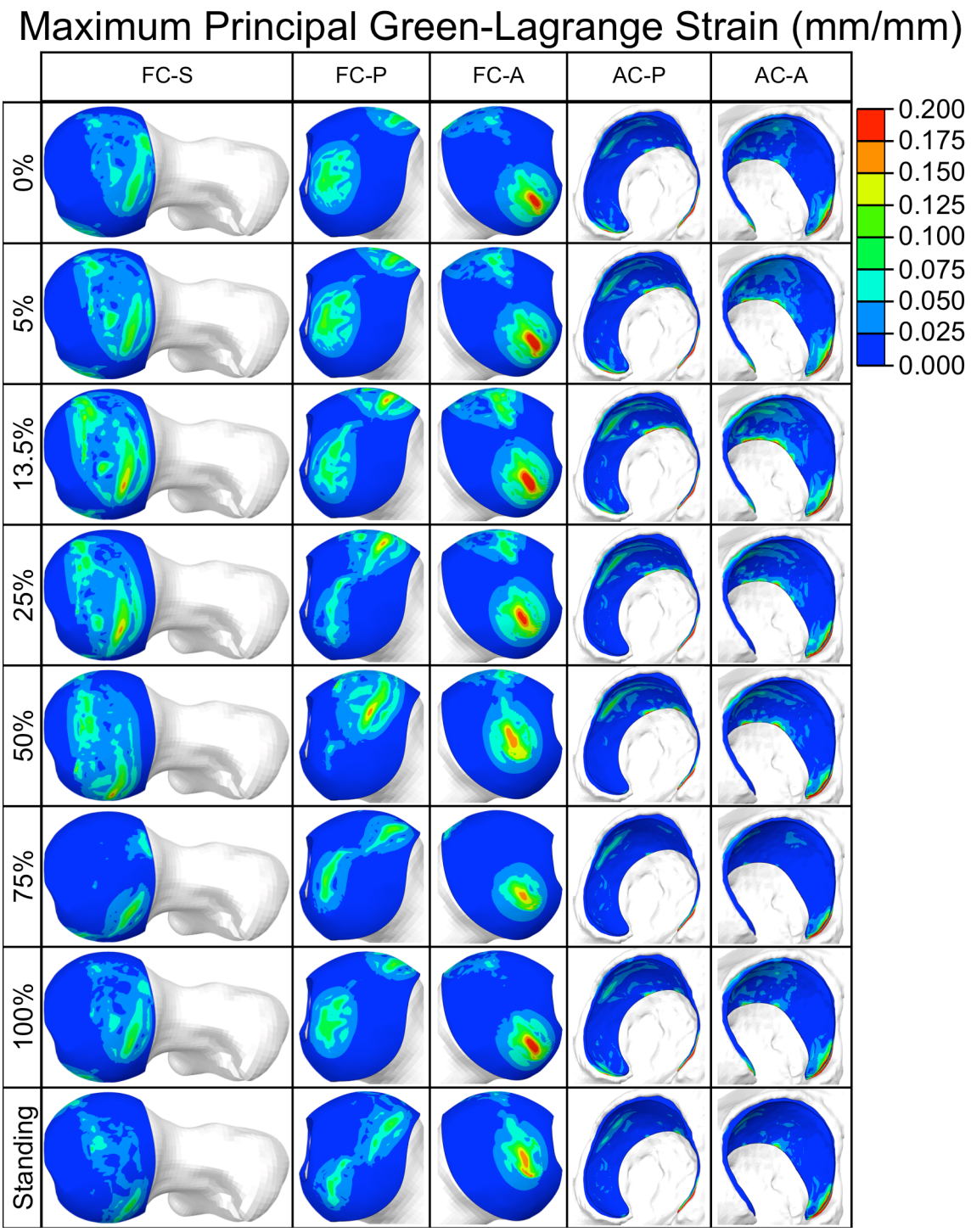

Figure 15. Contour plots of maximum principal Green-Lagrange strain at seven time points (% stance phase of gait cycle) and one for standing. Femoral cartilage is shown in superior (FC-S), posterior (FC-P), and anterior (FC-A) views and acetabular cartilage is shown in posterior (AC-P) and anterior (AC-A) views demonstrating a change in contact depending on % gait and standing.

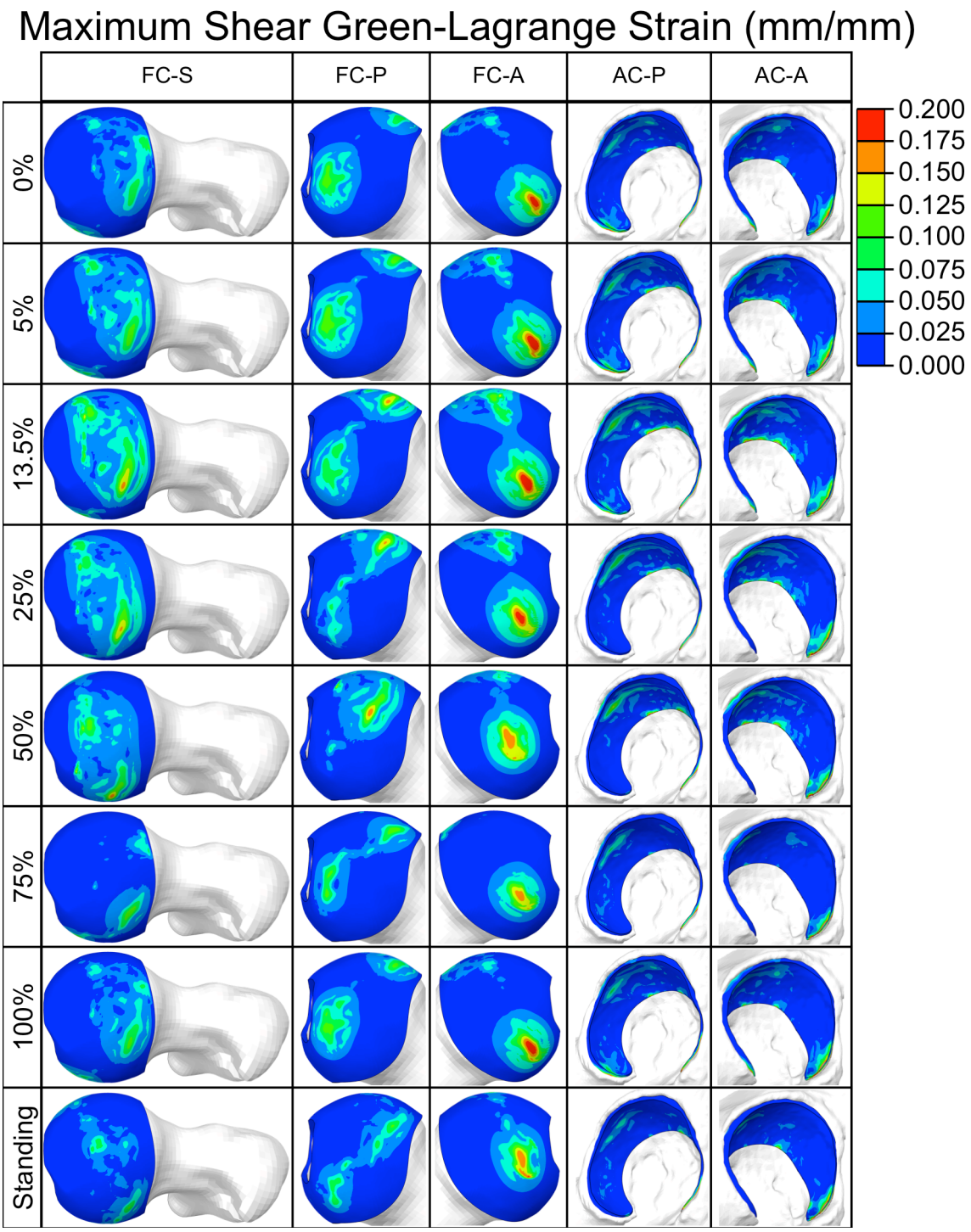

Figure 16. Contour plots of maximum shear Green-Lagrange strain at seven time points (% stance phase of gait cycle) and one for standing. Femoral cartilage is shown in superior (FC-S), posterior (FC-P), and anterior (FC-A) views and acetabular cartilage is shown in posterior (AC-P) and anterior (AC-A) views demonstrating a change in contact depending on % gait and standing.

CHAPTER 4

Discussion and Conclusions

4.1 Discussion

This FEM provides a foundation for continued research in developing a model to accurately predict OC stresses during specific activities. Numerous *in vitro* experimental studies provide a good agreement of contact pressures with which to validate this model. All experiments evaluated used a femur and pelvis from a cadaver. Most experiments used pressure-sensitive film located between articulating surfaces to measure pressures [3,4,5,8,84], with some using pressure transducers either embedded just below the surface of femoral cartilage [6], or cemented underneath the acetabular cartilage from behind [7]. Contact areas were either measured using pressure-sensitive film [3,84] or polyether casting [4].

4.1.1 Contact Pressure Validation

Peak contact pressures between 8.0 and 10.6 MPa agree favorably with multiple *in vitro* measurements: Anderson et al. reports peak pressures measured *in vitro* in excess of 10 MPa due to pressure measurement film detection limits [3]. Measurements made by von Eisenhart et al. report similar

results in two different studies, with peak pressures measured over 9 MPa [4] and up to 7.7 ± 1.95 MPa [5] for a load comparable to the peak load used in this model, which yielded a pressure of 10.6 MPa. Brown and Shaw reported experimental contact pressures around 7 MPa [6], for a load comparable to the peak load. Adams and Swanson also recorded similar contact pressures taken from cadaveric hips fitted with pressure transducers below the articular cartilage, finding peak pressures ranging from 5.26 to 8.57 MPa during normal walking loads [7]. Afoke et al. reported a contact pressure of 8.6 MPa [8] for a load similar to both the 5% and 50% gait loads used in this model, which yielded 9.9 and 10.0 MPa respectively. In addition to quantitative values, contact pressure distribution contours also compared favorably to *in vitro* studies [4,6,90,5,8,91]. These studies show similar banded contact distribution mostly in the superior region of the femoral head. However, a large amount of inter-subject variability has been observed in a study of 10 different subjects [57], making it somewhat difficult to compare contact pressure distribution between subjects. It is important to note that peak contact pressure on the femoral cartilage occurred at the edge of the acetabular cartilage for some time points. Since cartilage does not end abruptly but tapers off, this is an artifact of the geometry and is not anatomically accurate. Therefore, when this phenomenon occurred, it was ignored and the contact pressure in an area fully bounded by cartilage was recorded instead. Despite this observation, contact pressures agree favorably with published data for gait.

4.1.2 Contact Area Validation

This model predicted contact areas ranging from 576 mm^2 for 75% stance to 1010 mm^2 for 13.5% stance (peak load), with fair agreement with *in vitro* measurements: Anderson et al. found contact areas on the range of 322-425 mm^2 [3] for a load comparable to the 13.5% stance (peak load) in this study. Brown and Shaw measured contact areas of around 1500 mm^2 [6] for loads comparable to the peak load in this study. Konrath et al. reported a contact area of 546 mm^2 for a load comparable to 13.5% stance (peak load) [84]. However, uncertainty regarding the magnitude of the applied load used by Konrath et al. make it difficult to compare results directly and the study was designed to simulate single-leg standing instead of the stance phase of gait. In addition to the quantitative values discussed, contact area distributions also compared favorably to *in vitro* studies [4,6,90,5,8,91], which reported similar banded contact distribution in the superior lateral region of the acetabulum. However, as previously mentioned, it is difficult to compare pressure distribution due to variation between subjects [57]. To the author's knowledge, no other studies have attempted to quantify contact area during the stance phase of gait. Therefore, given the limited availability and large disagreement between contact areas in experimental data, contact area was more difficult to validate, which suggests some uncertainty with this and any FEMs of the hip joint. One reason for this lack of agreement in experimental data could be the difficulty in accurately measuring contact area during *in vitro* tests. Another possibility is that since individual anatomical measurements, such as the surface area of

acetabular cartilage, varies significantly among individuals [92], it is unsurprising that contact areas vary significantly across individuals as well. Inaccuracies in modeling surface geometry during this model's development can also affect contact behavior. Regardless, since the contact areas predicted by this model did fall within the range of the aforementioned experimental values, this model appears to be in fair agreement with *in vitro* measurements.

4.1.3 Strains

An important goal of this FEM is to evaluate strains in cartilage in order to predict OC damage. It is generally agreed that the mechanism of mechanical damage, such as cracking of the cartilage matrix, relates to maximum shear strain [89,31,93,32] or maximum principal (tensile) strain [31,33]. Therefore, contour plots of maximum principal and maximum shear strain were limited to 0.2 mm/mm (20%), since studies show that cartilage damage—both mechanical damage and cell death—generally begins occurring above this level [89,31]. However, since damage in cartilage is very complex and beyond the scope of this thesis, future considerations are discussed in the Future Work section. Strains computed throughout each cartilage region generally agreed with expected values for normal walking—generally below 15% for the highest loads. However, strains generally observed to cause cartilage damage are present in the anterior region of the acetabular cartilage in all load cases, with peak maximum principal strains reaching 148% and peak maximum shear strains at 100%. The corresponding region of the femoral cartilage also exhibited damaging strains, with peak maximum principal strains up to 39% and peak

maximum shear strains 34%. These high values are likely artifacts due to geometry contributions in the region, possibly a “high spot” in underlying subchondral bone, which agrees with past experimental studies showing that under-representing cartilage thickness results in higher strains and contact pressure [76]. Figure **17** shows a contour plot of strain in this region and a cross-section view of the cartilage thickness.

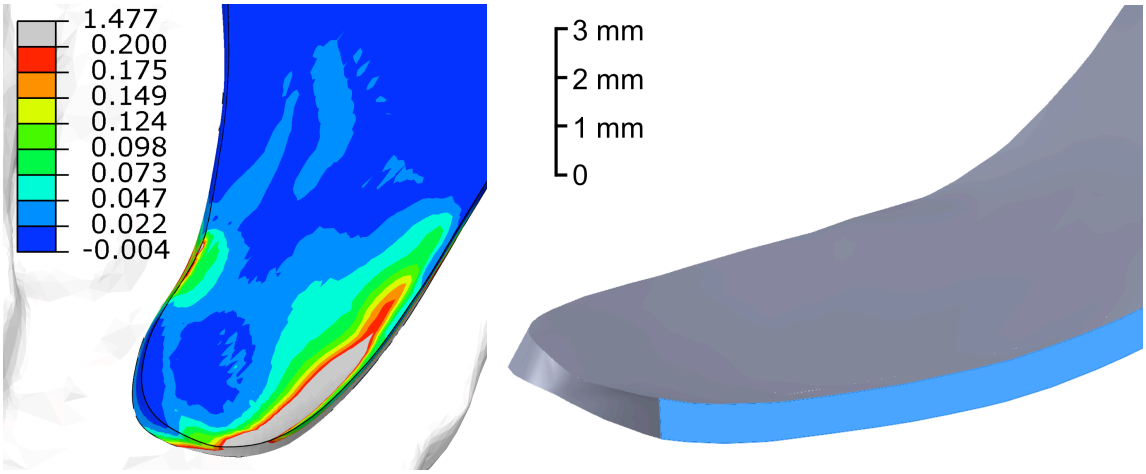

Figure 17. Contour plot of the anterior region of the acetabular cartilage showing unrealistic peak maximum principal strains up to 1.477 (148%, left). A SolidWorks solid model of the anterior region of acetabular cartilage (right) with a cross-section view of the thickness in light blue (acetabulum not shown). These peak strains likely an artifact resulting from under-representing cartilage thickness, which is less than 0.8 mm thick in some areas in this region.

Peak strains also occurred on the edge of the cartilage boundary. Strains along the boundary are likely overstated, since cartilage in these regions taper off more gradually, providing better support to limit excessive shearing of cartilage. Considering these factors, more reasonable peak strains were observed, with peak maximum principal strains up to 20% in acetabular cartilage and 26% in

femoral cartilage, and peak maximum shear strains of 17% in acetabular cartilage and 22% in femoral cartilage. Even considering these more realistic peak strains, strains in other regions of all time points generally did not exceed 20%, with most regions less than 10%. This agrees more reasonably with the understanding that loads during normal walking do not cause OC damage in healthy joints. Furthermore, it is not surprising that femoral cartilage has higher strains than acetabular cartilage, since femoral cartilage was assigned a lower elastic modulus than acetabular cartilage. Another important observation is that higher strains occurred on the subchondral bone boundary, rather than the articulating surface, which is inconsistent with experimental observations of cartilage damage [35]. Since cartilage is stiffest at the deep zone, higher strains develop in the superficial zone. However, these results showing higher strain in the deep zone are expected, since homogenous properties were used throughout the thickness of the cartilage and bones were assumed rigid.

Although contact pressures and areas vary in different experiments, the results are in good agreement with experimentally obtained values, given that work by Anderson, et al. suggests using rigid bones may produce nearly double contact pressures than models with deformable bones [94,3]. Regardless, given that contact pressures are in good agreement with the wide availability of experimental data from other studies, and that computed contact areas fall in the range of available published measurements, it is reasonable to assume this model is sufficiently validated during the stance phase of gait.

4.1.4 Comparison to Another Hip Joint FEM

Since input parameters and modeling techniques in this paper are similar to those used by Anderson et al. [3] to develop an FEM of the hip, this model lends itself well to closer comparison with their results. This thesis derived joint geometry from the CT image set Anderson et al. provided, from which they used to derive their own geometry and FE meshes [68], as well as using load and relative hip position data from the same dataset [46,45]. However, this thesis differs from Anderson's work in that it utilizes the significantly simpler material assumptions of rigid bones and linear elastic isotropic properties for cartilage. These changes greatly reduced computational cost. Even with those assumptions, the results compare favorably to those obtained by Anderson et al. who reported peak contact pressures of 10.8 MPa and a contact area of 304 mm^2 for gait, whereas this model predicted a peak contact pressure of 10.6 MPa and a contact area of 1010 mm^2 for 13.5% stance (peak load) in this study. Although both models report nearly identical contact pressures, a possible reason for the lower contact area reported by Anderson et al. might be their use of hyperelastic cartilage properties that stiffen for higher strains, effectively reducing the growth of the contact area as the load is applied. Anderson et al. did not report any OC tissue strains, so strains predicted by this FEM cannot be compared with their model.

4.2 Future Work

This model provides a good step toward developing techniques to evaluate how certain activities affect cartilage in individual subjects. However,

there are still a number of future considerations that may be evaluated in order to improve the accuracy of the results for gait simulations, as well as the validity of applying this model to other exercises and activities.

4.2.1 FEM Improvements

First, although cortical bone is roughly three orders of magnitude stiffer than cartilage, assuming rigid bones may produce higher stresses and smaller contact areas in comparison to experimentally measured values. A study examining the affects of a number of FE simplification assumptions of the hip joint has shown that using deformable cortical bone results in contact pressures in better agreement with *in vitro* measurements [94]. Therefore, cortical bones could be modeled as deformable, starting with using linear elastic isotropic material properties, and then, considering a more complex material model. In addition to modeling cortical bone, analysis should be performed to determine whether trabecular bone should be considered for inclusion as well. Additionally, modeling bone as deformable could provide an opportunity to study damage to subchondral bone, since certain impacts to the hip have been observed to cause damage to subchondral bone in addition to cartilage [89,93].

Second, in order to determine how different loading conditions contribute to cartilage damage, more accurate material models should be used to define cartilage. Although contact stress has been shown to be relatively insensitive to more accurate material models such as a neo-Hookean or Veronda Westmann models [58], studies have suggested transversely isotropic, linear, biphasic

constitutive models improve localized stress predictions consistent with failure testing [95]. However, to the author's knowledge this model has not been applied to anatomically accurate hip joints. Therefore continued work in this area is needed. Finally, the cartilage could be divided into three layers, more accurately representing its anatomy: the superficial zone, transitional zone, and deep zone, with appropriate material properties assigned to each. Using a more sophisticated constitutive model for cartilage should improve the accuracy of strain predictions through the depth of cartilage, including patterns of superficial to deep zone heterogeneities and provide more accurate predictions of tissue damage.

Third, cartilage geometry should be more closely inspected to ensure accurate surface extraction from CT images. Numerous estimations and manual mask editing procedures were required to discern areas where cortical bone, contrast agent, and cartilage regions blended together. CT image segmentation has been shown to vary even when the same individual interprets the same region [96]. It is possible some of these estimations were errant and could contribute to inaccurate geometry, which has been shown to be a large factor in contact pressure distributions [57]. A good step toward fixing any inaccuracies would be having a new researcher reevaluate the CT masks and geometry derivation in order to search for inconsistencies in trouble areas. Another option would be to derive geometry from higher resolution magnetic resonance images (MRI).

In addition to cartilage considerations, the biomechanical action of ligaments will need to be studied further in order to determine whether their contribution to cartilage stresses and strains is significant. It is possible that a method can be employed to minimize the model complexity of these tissues while still accurately representing their function, such as using one-dimensional spring elements [76].

Since a future goal for this FEM is to predict stresses and strains during exercise, including individual muscle contributions and locations in addition to a deformable bone model will likely improve the prediction of contact stresses and strains [97]. It will need to be determined how each muscle group should be represented, including number of attachment points, location and magnitude of each attachment point, and appropriate directional adjustment of each point in order to accurately represent the wide span of certain muscle attachments. Proper application of individual muscle forces will develop realistic joint contact forces for accurate modeling [98], and will be especially important with the inclusion of deformable bone material properties.

Finally, a major future goal for this FEM is to identify and recommend exercises that prevent or slow progression of OA in individuals with OC defects and/or improve treatment and rehabilitation of individuals treated with surgical interventions. Important future work could include modeling OC defects, modifying geometry to simulate the results of surgical procedures, or altering material properties in areas to simulate the change in material properties and

cartilage thickness due to OA [36,99] in order to study the effects of certain activities on the cartilage and subchondral bone and evaluate alternatives or recommend modification to those exercises. When combined with more advanced constitutive models for cartilage and subchondral bone, this model could provide a powerful tool for understanding the mechanics of OA progression.

4.2.2 Further Validation

A first step towards continuing development of this FEM for prediction of tissue stress and strain during exercise would be to expand validation of contact pressures and/or contact area to experimental measurements of other daily activities [3,100,101,51]. These activities lend themselves well for further validation of this FEM, since loads and angles for many common activities exist in the OrthoLoad database [45].

Furthermore, since a major goal of this research is to predict when and where OC damage occurs, a more comprehensive evaluation of the mechanisms contributing to damage is necessary in order to improve the model to accurately predict important variables. Specifically, a distinction between mechanical damage, such as cracking, and damage causing cell death or deactivation may be desirable in order to quantify what type of damage is occurring [38], although the actual mechanism of cell death is unknown [35].

Although the current FEM is only validated for one variable used extensively to define cartilage damage, contact pressures [35,13,36,34,102,99],

updating the model to report compressive strains normal to the articulating surface would provide an opportunity to compare results with studies that quantify damage in terms of compressive strains as well [34,13,36,37,103,99]. Further, since previous studies observe that strain rate, measured as a rate of compressive strain normal to the articulating surface, plays a significant role in mechanical damage [13,93,36,102,99], it is necessary to use strain rates when evaluating whether damage has occurred. Therefore, strain rates could be computed from loading magnitudes and times and used in conjunction with contact pressure and normal compressive strain to predict damage.

Since internal stresses and strains are important for identifying OC damage, which generally occurs near the articulating surface [35,37,32,93], the inclusion of deformable bone and depth-dependent cartilage constitutive properties could provide an opportunity for improvement and validation with experimental measurements of strain predictions through the depth of cartilage [104]. Further, extensive work aimed at understanding and classifying damage due to impact loading [102,89,31,37] could provide a potential opportunity to validate the model with an in-situ impact loading simulation. Parameters could be developed for evaluating whether a combination of strains and strain rates would generally cause cell death or mechanical damage.

4.3 Conclusion

The objective of this thesis was to develop a subject-specific FEM of the hip to predict tissue stresses and strains during the stance phase of gait. In short,

this model provides a validated tool for estimating contact pressures and contact areas in gait, reporting peak contact pressures ranging from 8.0 to 10.6 MPa and contact areas from 576 to 1010 mm^2. Although many simplifications were made, this model demonstrates good agreement with past experiments, and is therefore validated for the stance phase of gait. Additionally, since there are areas recognized for improvement and future work, the current model provides a foundation for developing a model that can be used to estimate osteochondral stresses and strains during various exercises for the purpose of prevention, treatment, and rehabilitation of osteoarthritis.

WORKS CITED

[1] XYZ Scientific Applications, Inc., TrueGrid, v. 2.3.4, www.truegrid.com.

[2] Dassault Systemes, ABAQUS, Simulia, v. 6.11-2, http://www.3ds.com/products-services/simulia/.

[3] A. E. Anderson et al., "Validation of finite element predictions of cartilage contact pressure in the human hip joint," *J. Biomech. Eng.*, vol. 130, pp. 1-10, Oct 2008.

[4] R. von Eisenhart et al., "Direct comparison of contact areas, contact stress and subchondral mineralization in human hip joint specimens," *Anat. Embryol.*, vol. 195, pp. 279-288, 1997.

[5] R. von Eisenhart et al., "Quantitative determination of joint incongruity and pressure distribution during simulated gait and cartilage thickness in the human hip joint," *J. Orthop. Res.*, vol. 17, pp. 532-539, 1999.

[6] T. D Brown and D. T. Shaw, "In vitro contact stress distributions in the natural human hip," *J. Biomech.*, vol. 16, no. 6, pp. 373-384, 1983.

[7] D. Adams and S. A. V. Swanson, "Direct measurement of local pressures in the cadaveric human hip joint during simulated level walking," *Ann. Rheum. Dis.*, vol. 44, pp. 658-666, 1985.

[8] N. Y. P. Afoke et al., "Contact pressures in the human hip joint," *J. Bone Jt. Surg.*, vol. 69-B, no. 4, pp. 536-541, Aug 1987.

[9] J. A. Buckwalter and H. J. Mankin, "Articular cartilage. Part I: Tissue design and chondrocyte-matrix interactions," *J. Bone Jt. Surg.*, vol. 79-A, no. 4, pp. 600-611, Apr 1997.

[10] A. Maroudas and M. Venn, "Chemical composition and swelling of normal and osteoarthrotic femoral head cartilage," *Ann. Rheum. Dis.*, vol. 36, pp. 399-406, 1977.

[11] V. C. Mow and A. Ratcliffe, "Structure and function of articular cartilage and meniscus," in *Basic Orthopaedic Biomechanics*, 2nd ed. Philadelphia, PA, USA: Lippincott-Raven Publishers, 1997, pp. 113-177.

[12] E. Yelin et al., "Medical care expenditures and earnings losses among persons with arthritis and other rheumatic conditions in 2003, and comparisons with 1997," *Arthritis Rheum.*, vol. 56, no. 5, pp. 1397-1407, 2007.

[13] T. M. Quinn et al., "Matrix and cell injury due to sub-impact loading of adult bovine articular cartilage explants: effects of strain rate and peak stress," *J. Orthop. Res.*, vol. 19, pp. 242-249, 2001.

[14] K. M. Flegal et al., "Prevalence and trends in obesity among US adults, 1999-2008," *J. Am. Med. Assoc.*, vol. 303, no. 3, pp. 235-241, Jan 2010.

[15] C. L. Ogden et al., "The epidemiology of obesity," *Gastroenterology*, vol. 132, pp. 2087-2102, 2007.

[16] D. T. Felson and Y. Zhang, "An update on the epidemiology of knee and hip osteoarthritis with a view to prevention," *Arthritis Rheum.*, vol. 41, no. 8, pp. 1343-1355, Aug 1998.

[17] C. Cooper et al., "Risk factors for the incidence and progression of radiographic knee osteoarthritis," *Arthritis Rheum.*, vol. 43, no. 5, pp. 995-1000, 2000.

[18] D. T. Felson et al., "Obesity and knee osteoarthritis: the Framingham study," *Ann. Intern. Med.*, vol. 109, pp. 18-24, Jul 1988.

[19] S. N. Issa and L. Sharma, "Epidemiology of osteoarthritis: An update," *Curr. Rheumatol. Rep.*, vol. 8, pp. 7-15, 2006.

[20] C. Cooper et al., "Individual risk factors for hip osteoarthritis: Obesity, hip injury, and physical activity," *Am. J. Epidemiol.*, vol. 147, no. 6, pp. 516-522, 1998.

[21] T. P., Mundermann, A. Andriacchi, "The role of ambulatory mechanics in the initiation and progression of knee osteoarthritis," *Curr. Opin. Rheumatol.*, vol. 18, no. 5, pp. 514-518, 2006.

[22] S. P. Messier et al., "Weight loss reduces knee-joint loads in overweight and obese older adults with knee osteoarthritis," *Arthritis Rheum.*, vol. 52, no. 7, pp. 2026-2032, 2005.

[23] A. E. Wluka et al., "The clinical correlates of articular cartilage defects in symptomatic knee osteoarthritis: A prospective study," *Rheumatol.*, vol. 44, pp. 1311-1316, 2005.

[24] L. Solomon, "Patterns of osteoarthritis of the hip," *J. Bone Jt. Surg.*, vol. 58-B, no. 2, pp. 176-183, May 1976.

[25] F. J. Blanco et al., "Osteoarthritis chondrocytes die by apoptosis," *Arth. Rheum.*, vol. 41, no. 2, pp. 284-289, Feb 1998.

[26] A. C. Gelber et al., "Joint injury in young adults and risk for subsequent knee and hip osteoarthritis," *Ann. Intern. Med.*, vol. 133, pp. 321-328, 2000.

[27] V. Morel and T. M. Quinn, "Cartilage injury by ramp compression near the gel diffusion rate," *J. Orthop. Res.*, vol. 22, pp. 145-151, 2004.

[28] N. E. Lane et al., "Association of mild acetabular dysplasia with an increased risk of incident hip osteoarthritis in elderly white women," *Arthritis Rheum.*, vol. 43, no. 2, pp. 400-404, Feb 2000.

[29] M. Beck et al., "Hip morphology influences the pattern of damage to the acetabular cartilage," *J. Bone Jt. Surg.*, vol. 87-B, pp. 1012-1018, 2005.

[30] T. D. Spector et al., "Genetic influences on osteoarthritis in women: A twin study," *Br. Med. J.*, vol. 312, pp. 940-944, Apr 1996.

[31] W. Wilson et al., "Causes of mechanically induced collagen damage in articular cartilage," *J. Orthop. Res.*, pp. 220-228, Feb 2006.

[32] A.W. Eberhardt et al., "An analytical model of joint contact," *J. Biomech. Eng.*, vol. 112, pp. 407-413, Nov 1990.

[33] P. A. Kelly and J. J. O'Conner, "Transmission of rapidly applied loads through articular cartilage. Part 1: Uncracked cartilage," *Proc. Instn. Mech. Engrs.*, vol. 210, pp. 27-37, 1996.

[34] R. U. Repo and J. B. Finlay, "Survival of articular cartilage after controlled impact," *J. Bone Jt. Surg.*, vol. 59, no. 8, pp. 1068-1076, 1977.

[35] C-T Chen et al., "Time, stress, and location dependent chondrocyte death and collagen damage in cyclically loaded articular cartilage," *J. Orthop. Res.*, vol. 21, pp. 888-898, 2003.

[36] B. Kurz et al., "Biosynthetic response and mechanical properties of articular cartilage after injurious compression," *J. Orthop. Res.*, vol. 19, pp. 1140-1146, 2001.

[37] P. A. Torzilli et al., "Effect of compressive strain on cell viability in statically loaded articular cartilage," *Biomechan. Model Mechanobiol.*, vol. 5, pp. 123-132, 2006.

[38] J. L. Lewis et al., "Cell death after cartilage impact occurs around matrix cracks," *J. Orthop. Res.*, vol. 21, pp. 881-887, 2003.

[39] G. D. Smith et al., "A clinical review of cartilage repair techniques," *J. Bone Jt. Surg.*, vol. 87-B, no. 4, pp. 445-449, Apr 2005.

[40] J. E. Browne and T. P. Branch, "Surgical alternatives for treatment of articular cartilage lesions," *J. Am. Acad. Orthop. Surg.*, vol. 8, pp. 180-189, 2000.

[41] J. A. Buckwalter and H. J. Mankin, "Articular cartilage repair and transplantation," *Arthritis Rheum.*, vol. 41, no. 8, pp. 1331-1342, Aug 1998.

[42] N. A. Sgaglione et al., "Update on advanced surgical techniques in the treatment of traumatic focal articular cartilage lesions in the knee," *J. Arthroscopic Rel. Surg.*, vol. 18, no. 2, pp. 9-32, Feb 2002.

[43] J. L. Koh et al., "The effect of graft height mismatch on contact pressure following osteochondral grafting," *Am. J. Sports Med.*, vol. 32, no. 2, pp. 317-320, 2004.

[44] J. A. Buckwalter and H. J. Mankin, "Articular cartilage: Part II: Degeneration and osteoarthrosis, repair, regeneration, and transplantation," *J. Bone Jt. Surg.*, vol. 79-A, no. 4, pp. 612-632, Apr 1997.

[45] Charité Universitaetsmedizin Berlin. (2008) Hip 98 Data.

[46] G. Bergmann et al., "Hip contact forces and gait patterns from routine activities," *J. Biomech.*, vol. 34, pp. 859–871, 2001.

[47] S. Park et al., "Hip muscle co-contraction: Evidence from concurrent in vivo pressure measurement and force estimation," *Gait and Posture*, vol. 10, pp. 211-222, 1999.

[48] B. W. Stansfield et al., "Direct comparison of calculated hip joint contact forces with those measured using instrumented implants. An evaluation of a three-dimensional mathematical model of the lower limb," *J. Biomech.*, vol. 36, pp. 929-936, 2003.

[49] R. Lewin, "Pressures measured in live hip joint," *Am. Assoc. Adv. Sci.*, vol. 232, no. 4755, pp. 1192-1193, Jun 1986.

[50] E. M. Strickland et al., "In vivo acetabular contact pressures during rehabilitation, part I: Acute phase," *Phys. Ther.*, vol. 72, no. 10, pp. 691-699, Oct 1992.

[51] S. J. Tackson et al., "Acetabular pressures during hip arthritis excercises," *Am. College Rheumatol.*, pp. 308-319, 1997.

[52] T. F. Boyd et al., "Pedal and knee loads using a multi-degree-of-freedom pedal platform in cycling," *J. Biomech.*, vol. 30, no. 5, pp. 505-511, 1997.

[53] M. Ericson, "On the biomechanics of cycling. A study of joint and muscle load during exercise on the bicycle ergometer," *Scand. J. Rehabil. Med. Suppl.*, vol. 16, pp. 1-43, 1986.

[54] C. S. Gregersen and M. L. Hull, "Non-driving intersegmental knee moments in cycling computed using a model that includes three-dimensional kinematics of the shank/foot and the effect of simplifying assumptions," *J. Biomech.*, vol. 36, pp. 803-813, 2003.

[55] K. M. Knutzen et al., "Influence of ramp position on joint biomechanics during elliptical trainer excercise," *Open Sports Sci. J.*, vol. 3, pp. 165-177, 2010.

[56] T. W. Lu et al., "Joint loading in the lower extermities during elliptical exercise," *Med. Sci. Sports Exercise*, vol. 39, pp. 1651-1658, 2007.

[57] M. D. Harris et al., "Finite element prediction of cartilage contact stresses in normal human hips," *J. Orthop. Res.*, pp. 1133-1139, Jul 2012.

[58] C. R. Henak et al., "Specimen-specific predictions of contact stress under physiological loading in the human hip: validation and sensitivity studies," *Biomech. Model Mechanobiology*, June 2013.

[59] H. Yoshida et al., "Three-dimensional dynamic hip contact area and pressure distribution during activities of daily living," *J. Biomech.*, no. 39, pp. 1996-2004, 2006.

[60] K. H. Shivanna et al., "Diarthrodial joint contact models: Finite element model development of the human hip," *Eng. Comp.*, vol. 24, pp. 155-163, 2008.

[61] F. Bachtar et al., "Finite element contact analysis of the hip joint," *Med. Bio. Eng. Comput.*, vol. 44, pp. 643-651, 2006.

[62] E. Genda et al., "Normal hip joint contact pressure distribution in single-leg standing--effect of gender and anatomic parameters," *J. Biomech.*, vol. 34, no. 34, pp. 895–905, 2001.

[63] J.P. Jorge et al., "Finite element studies of a hip joint with femoro-acetabular impingement of the cam type," *Comput. Meth. Biomech. Biomed. Eng.*, pp. 1-10, 2012.

[64] S. L. Delp et al., "OpenSim: Open-source software to create and analyze dynamic simulations of movement," *IEEE Trans. Biomed. Eng.*, vol. 54, no. 11, Nov 2007.

[65] Centers for Disease Control and Prevention. (2013, Dec) CDC web site. [Online]. http://www.cdc.gov/healthyweight/assessing/index.html

[66] P. DeVita and T. Hortobágyi, "Obesity is not associated with increased knee joint torque and power during level walking," *J. Biomech.*, vol. 36, pp. 1355-1362, 2003.

[67] K. R. Kaufman et al., "Gait characteristics of patients with knee osteoarthritis," *J. Biomech.*, vol. 34, pp. 907-915, 2001.

[68] University of Utah. Musculoskeletal Research Laboratories. [Online]. "http://mrl.sci.utah.edu/software/hip-image-data"

[69] D. E. T. Shepard and B. B. Seedhom, "The 'instantaneous' compressive modulus of human articular cartilage in joints of the lower limb," *Rheumatol.*, vol. 38, pp. 124-132, 1999.

[70] E. Peña et al., "A three-dimensional finite element analysis of the combined behavior of ligaments and menisci in the healthy human knee joint," *J. Biomec.*, vol. 39, pp. 1686-1701, 2006.

[71] T. L. Haut Donahue et al., "A finite element model of the human knee joint for the study of tibio-femoral contact," *J. Biomech. Eng.*, vol. 124, Jun 2002.

[72] C. G. Armstrong et al., "An analysis of the unconfined compression of articular cartilage," *J. Biomech. Eng.*, vol. 106, pp. 165-173, May 1984.

[73] A. F. Mak et al., "Biphasic indentation of articular cartilage-I. Theoretical analysis," *J. Biomech.*, vol. 20, no. 7, pp. 703-714, 1987.

[74] G. A. Ateshian et al., "Equivalence between short-time biphasic and incompressible elastic material responses," *J. Biomech. Eng.*, vol. 129, pp. 405-412, Jun 2007.

[75] D. L. Bartel et al., *Orthopaedic Biomechanics*, 1st ed., Holly Stark, Ed. Upper Saddle River, NJ, USA: Pearson Prentice Hall, 2006.

[76] G. Li et al., "Variability of a 3-dimensional finite element model constructed using magnetic resonance images of a knee for joint contact stress analysis," *J. Biomech. Eng.*, vol. 123, pp. 341-346, Aug 2001.

[77] H. D. Martin et al., "The function of the hip capsular ligaments: A quantitative report," *Arthroscopy: J. Arthroscopic Related Surg.*, vol. 24, no. 2, pp. 188-195, Feb 2008.

[78] F. K. Fuss and A. Bacher, "New aspects of the morphology and function of the human hip joint ligaments," *Am. J. Anat.*, vol. 192, pp. 1-13, 1991.

[79] S. J. Ferguson et al., "An in vitro investigation of the acetabular labral seal in hip joint mechanics," *J. Biomech.*, vol. 36, pp. 171-178, 2003.

[80] G. A. Ateshian et al., "The role of interstitial fluid pressurization and surface porosities on the boundary friction of articular cartilage," *J. Tribol.*, vol. 120, no. 2, pp. 241-251, 1998.

[81] H. Forster and J. Fisher, "The influence of loading time and lubricant on the friction of articular cartilage," in *Proc. Institution of Mechanical Engineering*, vol. 210, 1996, pp. 109-119.

[82] S. Park et al., "Cartilage interstitial fluid load support in unconfined compression," *J. Biomech.*, vol. 36, pp. 1785-1796, 2003.

[83] S. J. Ferguson et al., "The influence of the acetabular labrum on hip joint cartilage consolidation: A poroelastic finite element model," *J. Biomech.*, vol. 33, pp. 953-960, 2000.

[84] G.A. Konrath et al., "The role of the acetabular labrum and the transverse acetabular ligament in load transmission in the hip," *J. Bone Jt. Surg.*, vol. 80-A, no. 12, pp. 1781-1788, Dec 1998.

[85] C. R. Henak et al., "Role of the acetabular labrum in load support across the hip joint," *J. of Biomech.*, vol. 44, pp. 2201-2206, 2011.

[86] Materialise, Mimics, v. 16.0, http://biomedical.materialise.com/mimics.

[87] Dassault Systemes, SolidWorks, v. 2011, http://www.3ds.com/products-services/solidworks/.

[88] V. C. Mow and G. A. Ateshian, "Lubrication and wear of diarthrodial joints," in *Basic Orthopaedic Biomechanics*, 2nd ed. Philadelphia, PA, USA: Lippincott-Raven Publishers, 1997, pp. 286-291.

[89] J. E. Jeffrey et al., "Matrix damage and chondrocyte viability following a single impact load on articular cartilage," *Arch. Biochem. and Biophys.*, vol. 322, no. 1, pp. 87-96, Sep 1995.

[90] B. K. Bay et al., "Statically equivalent load and support conditions produce different hip joint contact pressures and periacetabular strains," *J. Biomech.*, vol. 30, no. 2, pp. 193-196, 1997.

[91] P. D. Rushfeld et al., "Influence of cartilage geometry on the pressure distribution in the human hip joint," *Am. Assoc. Adv. Sci.*, vol. 204, no. 27, pp. 413-415, Apr 1979.

[92] F. Eckstein et al., "Quantitative analysis of incongruity, contact areas and cartilage thickness in the human hip joint," *Acta Anat.*, vol. 158, pp. 192-204, 1997.

[93] H. Silyn-Roberts and N. D. Broom, "Fracture behaviour of cartilage-on-bone in response to repeated impact loading," *Connect. Tissue Res.*, vol. 24, pp. 143-156, 1990.

[94] A. E. Anderson et al., "Effects of idealized joint geometry on finite element predictions of cartilage contact stresses in the hip," *J. Biomech.*, vol. 43, pp. 1351–1357, 2010.

[95] P. S. Donzelli et al., "Contact analysis of biphasic transversely isotropic cartilage layers and correlations with tissue failure," *J. Biomech.*, vol. 32, pp. 1037-1047, 1999.

[96] B. C. Allen et al., "Acetabular cartilage thickness: Accuracy of three-dimensional reconstructions from multidetector CT arthrograms in a cadaver study," *Radiology*, vol. 255, no. 2, pp. 544-552, May 2010.

[97] G. N. Duda et al., "Influence of muscle forces on femoral strain distribution," *J. Biomech.*, vol. 31, pp. 841-846, 1998.

[98] T. A. Correa et al., "Contributions of individual muscles to hip joint contact force in normal walking," *J. Biomech.*, vol. 43, pp. 1618-1622, 2010.

[99] M. Thibault et al., "Cyclic compression of cartilage/bone explants in vitro leads to physical weakening, mechanical breakdown of collagen and release of matrix fragments," *J. Orthop. Res.*, vol. 20, pp. 1265-1273, 2002.

[100] W. A. Hodge et al., "Contact pressures from an instrumented hip endoprosthesis," *J. Bone Jt. Surg.*, vol. 71, no. 9, pp. 1378-1386, Oct 1989.

[101] D. E. Krebs et al., "Excercise and gait effects on in vivo hip contact pressures," *J. Am. Phys. Ther. Assoc.*, vol. 71, pp. 301-309, 1991.

[102] B. J. Ewers et al., "The extent of matrix damage and chondrocyte death in mechanically traumatized articular cartilage explants depends on rate of loading," *J. Orthop. Res.*, vol. 19, pp. 779-784, 2001.

[103] J. B. Finlay and R. U. Repo, "Instrumentation and procedure for the controlled impact of articular cartilage," *IEEE Trans. Biomed. Eng.*, vol. BME-25, no. 1, pp. 34-39, Jan 1978.

[104] F. Guilak et al., "Chondrocyte deformation and local tissue strain in articular cartilage: A confocal microscopy study," *J. Orthop. Res.*, vol. 13, pp. 410-421, 1995.

APPENDICES

Appendix A: User subroutine to define principal Green-Lagrange strains

```
      SUBROUTINE UVARM(UVAR,DIRECT,T,TIME,DTIME,CMNAME,ORNAME,
     1              NUVARM,NOEL,NPT,NLAYER,NSPT,KSTEP,KINC,
     2              NDI,NSHR,COORD,JMAC,JMATYP,MATLAYO, LACCFLG)
C
      INCLUDE 'ABA_PARAM.INC'
C
      CHARACTER*80 CMNAME,ORNAME
      DIMENSION UVAR(6),TIME(2),DIRECT(3,3),T(3,3),COORD(*),
     $     JMAC(*),JMATYP(*)
C     USER DEFINED DIMENSION STATEMENTS
      CHARACTER*3 FLGRAY(15)
      DIMENSION ARRAY(15),JARRAY(15)
C     DIMENSION LE1(1),LE2(1),LE3(1),LAM1(1),LAM2(1),LAM3(1)
C
C     The dimensions of the variables ARRAY and JARRAY
C     must be set equal to or greater than 15
C
      CALL GETVRM('LEP',ARRAY,JARRAY,FLGRAY,JRCD,
     $     JMAC,JMATYP,MATLAYO, LACCFLG)
C
C  Calculate principal stretches from LE, then calculate Green-Lagrange
C  strains from principal stretches. Also calculate max shear strain
C
      UVAR(1)=.5*((2.718282**ARRAY(1))**2-1)
      UVAR(2)=.5*((2.718282**ARRAY(2))**2-1)
      UVAR(3)=.5*((2.718282**ARRAY(3))**2-1)
      UVAR(4)=(UVAR(3)-UVAR(1))/2
C
      RETURN
      END
```

Appendix B: Table of minimum principal Green-Lagrange strain

Table 12. Peak minimum principal Green-Lagrange strain recorded for each time point (% stance phase of gait cycle), as well as for standing.

	Stance Phase of Gait							
	0%	5%	13.5% (Peak load)	25%	50%	75%	100%	Standing
Acetabular Cartilage (max reported)	-0.502	-0.515	-0.499	-0.451	-0.530	-0.494	-0.510	-0.533
Acetabular Cartilage (true max)	-0.098	-0.119	-0.145	-0.117	-0.147	-0.097	-0.108	-0.079
Femoral Cartilage (max reported)	-0.281	-0.203	-0.210	-0.196	-0.191	-0.181	-0.218	-0.191
Femoral Cartilage (true max)	-0.190	-0.168	-0.181	-0.173	-0.177	-0.127	-0.128	-0.123